Khakalo, Sergei; Niiranen, Jarkko

Anisotropic strain gradient thermoelasticity for cellular structures : plate models, homogenization and isogeometric analysis

Published in:
Journal of the Mechanics and Physics of Solids

DOI:
10.1016/j.jmps.2019.103728

Published: 01/01/2020

Document Version
Peer-reviewed accepted author manuscript, also known as Final accepted manuscript or Post-print

Journal Pre-proof

Anisotropic strain gradient thermoelasticity for cellular structures: plate models, homogenization and isogeometric analysis

Sergei Khakalo, Jarkko Niiranen

PII: S0022-5096(19)30625-8
DOI: https://doi.org/10.1016/j.jmps.2019.103728
Reference: MPS 103728

To appear in: *Journal of the Mechanics and Physics of Solids*

Received date: 4 July 2019
Revised date: 28 August 2019
Accepted date: 13 September 2019

Please cite this article as: Sergei Khakalo, Jarkko Niiranen, Anisotropic strain gradient thermoelasticity for cellular structures: plate models, homogenization and isogeometric analysis, *Journal of the Mechanics and Physics of Solids* (2019), doi: https://doi.org/10.1016/j.jmps.2019.103728

Anisotropic strain gradient thermoelasticity for cellular structures: plate models, homogenization and isogeometric analysis

Sergei Khakalo[a,b,1], Jarkko Niiranen[b,c]

[a] *VTT Technical Research Centre of Finland, P.O.Box 1000, Espoo, Finland.*
[b] *Aalto University, School of Engineering, Department of Civil Engineering, P.O. Box 12100, 00076 AALTO, Finland.*
[c] *Technische Universität München, Department of Civil, Geo and Environmental Engineering, Chair for Computation in Engineering, Germany.*

Abstract

For three-dimensional cellular plate-like structures with a triangular (extruded lattice) microarchitecture, the article develops a pair of two-scale plate models relying on the anisotropic form of Mindlin's strain gradient thermoelasticity theory. Accordingly, a computational homogenization method is proposed for determining the constitutive parameters of the related higher-order constitutive tensors. First, a Reissner–Mindlin plate model is derived by dimension reduction from a general framework of three-dimensional orthotropic strain gradient thermoelasticity and written as a variational formulation. An isogeometric conforming Galerkin method is formulated accordingly. Second, the plate model is modified in order to reduce the number of the constitutive strain gradient parameters. These steps are then repeated by following the kinematical assumptions of the Kirchhoff plate theory. Third, in order to see the cellular microarchitecture as a homogeneous three-dimensional material with classical modulae of transversal isotropy, classical computational homogenization is accomplished for determining the corresponding material parameters. Fourth, in order to see the cellular structures as two-dimensional plates, a non-classical homogenization procedure is proposed for the identification of the strain gradient modulae of the plate models. Finally, a set of numerical examples illustrates the reliability and efficiency of the resulting plate models in homogenizing cellular plate-like

[1]Corresponding author, sergei.khakalo@vtt.fi

structures into strain gradient plate models capturing the bending size effects induced by the microarchitecture.

Keywords: Cellular plates, Lattice microarchitecture, Strain gradient thermoelasticity, Reissner–Mindlin plate, Kirchhoff plate, Size effects, Isogeometric analysis

---

1. Introduction

From the days of the industrial revolution, the ability to design, engineer and manufacture a desired material microstructure has been a key to the development of new materials and enhanced, or even extraordinary, material properties. The sprouts of today's physics, materials science and engineering manifest that the material substance of the future solids and structures will be fundamentally more diverse and versatile than that of the current counterparts. Cellular or lattice metamaterials, specifically, from nano- and micro-scales onwards [1, 2, 3, 4, 5, 6] and often inspired by nature [7], have become an extremely promising class of lightweight, functional metamaterials [8, 9, 10, 11]. This has primarily followed from the rapid development of additive manufacturing technologies for different parent materials and across the scales [1, 6, 9]. The extreme fundamental properties of lattice architectures have increased the attractiveness of this class of metamaterials as well. Indeed, high and adjustable stiffness-to-weight, strength-to-weight and surface-to-volume ratios as well as high ductility [12, 8, 9, 11] and band gaps in wave propagation [13, 14, 15, 16] make different kinds of lattices apt for a variety of applications in machines, vehicles, buildings or bioproducts, e.g., in the form of lightweight parts, dampers, absorbers, insulators, heat exchangers and filters [12, 17, 8, 9, 11]. The large variety of applications stems from the diversity and versatility of different lattice types provide for the architected material heterogeneity, typically categorized in the following ways [12, 8, 9, 11]: open-cell (truss) or closed-cell (web/plate/shell) lattices; periodic (topology, shape and size fixed), pseudoperiodic (fixed topology but different shapes and sizes), disordered or randomized lattices (different topologies, shapes and cell sizes); homogeneous or heterogeneous lattices (constant or varying/gradual strut/shell thickness); nonhierarchical or hierarchical (possibly fractal) lattices.

Modeling the physics and mechanics of solids and structures with lattice microarchitecture is neither trivial nor computationally cheap for several reasons. Even for the most fundamental case of modelling one single lattice cell, i.e., a representative volume element (RVE) basically serving periodic lattices, there are several hindrances [18, 12]: a large number of nodes or intersection domains connecting structural members (struts or cell walls); bar/beam or plate/shell models are inaccurate for relative lattice densities greater than one percent [4]; most of the theoretical results [3] are not valid for higher relative lattice densities [4]; parent material size effects (at nano-scale, in particular) [19, 20]; parent material microstructure and imperfections resulting from manufacturing processes [21, 22, 23]. For microarchitecture solids and structures with graduality or hierarchy, there are many additional obstacles: full-field 3D solid models, even for node/intersection modeling alone [24], are extremely costly; bar/beam or plate/shell models are computationally costly at least in 3D [25]; complex spatial configurations lead to favoring the simplest cases of analysis. The simplest cases mean the following: 2D configurations and periodic lattices [26, 17]; truss lattices with simple structural models (bars or beams) [27]; standard (computational) continuum homogenization for RVEs [28]. Designing extraordinary metamaterial properties, in particular, might require peculiar topologies and hence either detailed and extremely costly full-field models or multi-scale continuum models. With respect to this direction, the following obstacles can be recognized: size effects [25, 29, 30, 31, 32] or band gaps [13, 14, 16, 33, 10] are not captured by the standard Cauchy continuum; extraordinary metamaterial properties might be ruled by internal or boundary layers of higher strain gradients [34, 35, 36]; size effects dominate thin structures having a microarchitecture (thickness comparable to cell size) [31, 25, 29].

This article focuses on the theoretical and numerical physico-mathematical modeling of thin and thick plate structures composed of a cellular microarchitecture metamaterial. The thermomechanical modelling of this type of microarchitectural structures is accomplished in the framework of orthotropic strain gradient thermoelasticity. More precisely, a plane triangular regular lattice is extruded in the third spatial coordinate direction in order to form a cellular metamaterial. Transversally isotropic plate structures with different thicknesses are made of this metamaterial in the following manner of transversal stacking, uniaxial repetition and extrusion: when viewing from the extrusion direction, the lateral face of the plate looks like a triangular truss (for the thickness of one single triangular cell) or a stack of triangular trusses (for the thicknesses of more than two triangular cells), see Fig. 6.2. In particular, our focus is on the modeling of the size effects of thermal and mechanical bending – with size effects, we refer to the number of cells in the thickness direction. In essence, it is shown that with anisotropic generalized plate models of the Kirchhoff and Reissner–Mindlin types – dimensionally reduced from a three-dimensional orthotropic Mindlin type strain gradient solid [37] – the size-dependent mechanical bending of thin and thick plates is captured in a theoretically novel and computationally efficient way. Mechanical and thermal bending of plane beams with the triangular microarchitecture has been recently studied in [25, 29]. In general, it should be pointed out that different microarchitectures or structural deformation states cannot be captured with one single generalized continuum description: in the chosen triangular microarchitecture in structural bending, internal rotational degrees of freedom are inactive (the cellular web is in a stretching-dominated deformation state) opposite to modeling granular materials, for instance, for which Cosserat-type continua seem to be a proper choice [38, 39].

Literature on homogenization towards generalized continua is still quite limited: there exist contributions for general principles [40, 41, 42], for the Cosserat continuum [43, 44], for micromorphic media [45, 46, 47, 48], and for higher gradient continua [49, 50, 51, 31, 25, 14]. Most importantly, only a few works on strain gradient continuum mechanics proposes generalized homogenization methods [49, 51, 25, 14, 52, 53] for determining the constitutive parameters of the higher-order constitutive tensor pairing the strain gradients and their dual variables, the double forces. Literature on generalized continua in general is already vast, especially for the derivations, formulations and parameters studies on thin structures and plane problems (see [44, 54, 55, 56, 57, 58, 59, 60, 61, 62] and [63, 64, 65, 31, 66], respectively, and the references therein). For modeling microarchitectures by generalized continuum models, literature is more limited [67, 68, 35, 36, 25, 29, 14] – especially for modelling anisotropic microarchitectures requiring richer constitutive laws than the limited ones of gradient elasticity with separable weak non-locality [69, 70, 71] (having origins in the works of Aifantis and co-workers [72, 73, 74] considering one single length scale parameter).

The present work proposes a computational homogenization method for determining the required set of non-classical material parameters of the higher-order constitutive tensor (acting on the gradients of the curvature tensor and shear vector) by generalizing the method proposed in [25] for uniaxial beam bending. The approach relies on matching the global responses of full-field simulations with the corresponding ones of the chosen generalized plate model for a representative family of simple test problems.

The material parameters of the classical elasticity tensor are determined by the techniques of classical computational homogenization [75] and then reduced to the plane stress counterparts of the plate model (acting on the curvature tensor and shear vector). For the generalized plate models – derived here for the first time for orthotropic thermoelasticity – isogeometric conforming Galerkin methods are utilized (cf. [63, 58, 64, 59, 60, 61, 62]), while the computational model validation is based on full-field finite element analysis with standard solid elements. The core novelties of the work can be listed as follows: (i) a formulation of a Mindlin-type orthotropic three-dimensional strain gradient thermoelasticity theory; (ii) the corresponding Kirchhoff and Reissner–Mindlin plate models and their constitutively reduced versions (with four higher-order material parameters); (iii) a computational homogenization method for determining the higher-order constitutive parameters; (iv) demonstrations for the reliability and efficiency of the computationally light generalized plate models and isogeometric Galerkin methods in capturing the bending size effects induced by the microarchitecture of cellular plate-like structures.

The rest of the article is organized as follows: Section 2 formulates the orthotropic strain gradient thermoelasticity theory. Sections 3 and 4 derive the corresponding plate models with variational formulations and conforming Galerkin formulations. Section 5 focuses on the classical computational homogenization, whereas Section 6 introduces the homogenization procedure for determining the higher-order elastic modulae. Section 7 consists of examples considering both mechanical and thermal bending. Some of the mathematical and numerical details are reported in the Appendices.

2. Orthotropic strain gradient thermoelasticity

By following the principle of virtual work (PVW) $\delta W_{int} = \delta W_{ext}$, the variation of the internal, or strain, energy stored in a second grade solid can be written as [37]

$$\delta W_{int} = \int_{\mathcal{B}} (\sigma_{ij}\delta\varepsilon_{ij} + \mu_{ijk}\delta\eta_{ijk})\mathrm{d}\mathcal{B}, \quad i,j,k = 1,2,3 \tag{2.1}$$

where $\mathcal{B}$ is a volume occupying the solid in a three-dimensional (3D) space, σ_{ij} and ε_{ij} denote, respectively, the components of the Cauchy stress and strain tensors, whereas μ_{ijk} and η_{ijk} stand, accordingly, for the components of the double stress and strain gradient tensors. The strain tensor being the symmetric part of the displacement gradient and the strain gradient tensor can be formally expressed in the following component form:

$$\varepsilon_{ij} = (u_{j,i} + u_{i,j})/2, \quad \eta_{ijk} = \varepsilon_{ij,k} = (u_{j,ik} + u_{i,jk})/2. \tag{2.2}$$

For centrosymmetric second grade thermoelastic materials, constitutive equations are written in the form of the classical and generalized [29] Duhamel–Neumann laws

$$\sigma_{ij} = C_{ijkl}(\varepsilon_{kl} - \varepsilon^{\theta}_{kl}), \tag{2.3}$$

$$\mu_{ijk} = A_{ijklmn}(\eta_{lmn} - \eta^{\theta}_{lmn}), \tag{2.4}$$

where C_{ijkl} and A_{ijklmn} stand, respectively, for the components of fourth and sixth rank stiffness tensors (see [76] for symmetry conditions). The expressions in parentheses in (2.3) and (2.4) denote the elastic parts of strains and strain gradients, accordingly, while $\varepsilon^{\theta}_{ij}$ and η^{θ}_{ijk} stand, respectively, for the components of the classical thermal eigenstrain tensor and its higher-order counterpart. By explicitly writing the components of the classical thermal eigenstrain and recalling the second expression in (2.2), the higher-order thermal counterpart takes the form

$$\varepsilon^{\theta}_{ij} = \theta\alpha_{ij}, \quad \eta^{\theta}_{ijk} = \varepsilon^{\theta}_{ij,k} = (\theta\alpha_{ij})_{,k}, \tag{2.5}$$

where α_{ij} are thermal expansion coefficients and θ denotes the temperature change. The constitutive equations (2.3) and (2.4), respectively, can be rewritten in the form

$$\sigma_{ij} = C_{ijkl}(\varepsilon_{kl} - \theta\alpha_{kl}), \quad \mu_{ijk} = A_{ijklmn}(\varepsilon_{lm} - \theta\alpha_{lm})_{,n}, \tag{2.6}$$

where it is explicitly seen that the elastic part of the higher-order state variable is nothing but the gradient of the classical elastic strains. This is compatible with a situation where constant or linear temperature changes produce zero stresses (both Cauchy and double) in a body made of a homogeneous material and experiencing zero loadings.

By utilizing the Voigt notation, the constitutive equation (2.3) for orthotropic materials can be represented as

$$\begin{bmatrix} \boldsymbol{\sigma}^1 \\ \boldsymbol{\sigma}^2 \end{bmatrix} = \begin{bmatrix} \hat{\mathbf{C}}^1 & \mathbf{0} \\ \mathbf{0} & \hat{\mathbf{C}}^2 \end{bmatrix} \begin{bmatrix} \boldsymbol{\varepsilon}^1 - \boldsymbol{\varepsilon}^{\theta} \\ \boldsymbol{\varepsilon}^2 - \mathbf{0} \end{bmatrix}, \tag{2.7}$$

where different stress and strain vectors and constitutive matrices are defined as

$$\boldsymbol{\sigma}^1 = \begin{bmatrix} \sigma_{xx} \\ \sigma_{yy} \\ \sigma_{zz} \\ \sigma_{xy} \end{bmatrix}, \ \boldsymbol{\sigma}^2 = \begin{bmatrix} \sigma_{yz} \\ \sigma_{xz} \end{bmatrix}, \ \boldsymbol{\varepsilon}^1 = \begin{bmatrix} \varepsilon_{xx} \\ \varepsilon_{yy} \\ \varepsilon_{zz} \\ \gamma_{xy} \end{bmatrix}, \ \boldsymbol{\varepsilon}^\theta = \theta \begin{bmatrix} \alpha_{xx} \\ \alpha_{yy} \\ \alpha_{zz} \\ 0 \end{bmatrix}, \ \boldsymbol{\varepsilon}^2 = \begin{bmatrix} \gamma_{yz} \\ \gamma_{xz} \end{bmatrix}, \tag{2.8}$$

$$\hat{\mathbf{C}}^1 = \begin{bmatrix} \hat{C}_{11} & \hat{C}_{12} & \hat{C}_{13} & 0 \\ \hat{C}_{12} & \hat{C}_{22} & \hat{C}_{23} & 0 \\ \hat{C}_{13} & \hat{C}_{23} & \hat{C}_{33} & 0 \\ 0 & 0 & 0 & \hat{C}_{66} \end{bmatrix}, \quad \hat{\mathbf{C}}^2 = \begin{bmatrix} \hat{C}_{44} & 0 \\ 0 & \hat{C}_{55} \end{bmatrix}. \tag{2.9}$$

For orthotropic materials which are described by nine (9) independent classical elastic moduli with units of force per area, it is convenient to split the constitutive relation (2.3) into two parts such that shear stresses with respect to z-coordinate are separated.

Within second grade elasticity, the higher-order stiffness tensor of orthotropic solids brings fifty one (51) additional elastic moduli. For the constitutive law (2.4) corresponding to double stresses, we utilize the analogue of the Voigt notation proposed in [77] and extend it towards thermoelasticity as

$$\begin{bmatrix} \boldsymbol{\mu}^1 \\ \boldsymbol{\mu}^2 \\ \boldsymbol{\mu}^3 \\ \boldsymbol{\mu}^4 \end{bmatrix} = \begin{bmatrix} \hat{\mathbf{A}}^1 & \mathbf{0} & \mathbf{0} & \mathbf{0} \\ \mathbf{0} & \hat{\mathbf{A}}^2 & \mathbf{0} & \mathbf{0} \\ \mathbf{0} & \mathbf{0} & \hat{\mathbf{A}}^3 & \mathbf{0} \\ \mathbf{0} & \mathbf{0} & \mathbf{0} & \hat{\mathbf{A}}^4 \end{bmatrix} \begin{bmatrix} \boldsymbol{\eta}^1 - \boldsymbol{\eta}^1_\theta \\ \boldsymbol{\eta}^2 - \boldsymbol{\eta}^2_\theta \\ \boldsymbol{\eta}^3 - \boldsymbol{\eta}^3_\theta \\ \boldsymbol{\eta}^4 - \mathbf{0} \end{bmatrix}, \tag{2.10}$$

where the matrix of the higher-order moduli is block-diagonal. In this case, the constitutive equation is split into four parts in which the double stress conponents are combined as follows:

$$\boldsymbol{\mu}^1 = \begin{bmatrix} \mu_{xxx} \\ \mu_{yyx} \\ \mu_{xyy} \\ \mu_{zzx} \\ \mu_{xzz} \end{bmatrix}, \quad \boldsymbol{\mu}^2 = \begin{bmatrix} \mu_{yyy} \\ \mu_{xxy} \\ \mu_{xyx} \\ \mu_{zzy} \\ \mu_{yzz} \end{bmatrix}, \quad \boldsymbol{\mu}^3 = \begin{bmatrix} \mu_{zzz} \\ \mu_{xxz} \\ \mu_{xzx} \\ \mu_{yyz} \\ \mu_{yzy} \end{bmatrix}, \quad \boldsymbol{\mu}^4 = \begin{bmatrix} \mu_{xyz} \\ \mu_{xzy} \\ \mu_{yzx} \end{bmatrix}. \tag{2.11}$$

The corresponding components of the strain gradient tensor are collected as

$$\boldsymbol{\eta}^1 = \begin{bmatrix} \varepsilon_{xx,x} \\ \varepsilon_{yy,x} \\ \varepsilon_{xy,y} \\ \varepsilon_{zz,x} \\ \varepsilon_{xz,z} \end{bmatrix}, \quad \boldsymbol{\eta}^2 = \begin{bmatrix} \varepsilon_{yy,y} \\ \varepsilon_{xx,y} \\ \varepsilon_{xy,x} \\ \varepsilon_{zz,y} \\ \varepsilon_{yz,z} \end{bmatrix}, \quad \boldsymbol{\eta}^3 = \begin{bmatrix} \varepsilon_{zz,z} \\ \varepsilon_{xx,z} \\ \varepsilon_{xz,x} \\ \varepsilon_{yy,z} \\ \varepsilon_{yz,y} \end{bmatrix}, \quad \boldsymbol{\eta}^4 = \begin{bmatrix} \varepsilon_{xy,z} \\ \varepsilon_{xz,y} \\ \varepsilon_{yz,x} \end{bmatrix}. \tag{2.12}$$

The components of higher-order temperature strain tensor, or the gradient of the temperature strain tensor, are collected in the form

$$\boldsymbol{\eta}_\theta^1 = \begin{bmatrix} (\theta\alpha_{xx})_{,x} \\ (\theta\alpha_{yy})_{,x} \\ 0 \\ (\theta\alpha_{zz})_{,x} \\ 0 \end{bmatrix}, \quad \boldsymbol{\eta}_\theta^2 = \begin{bmatrix} (\theta\alpha_{yy})_{,y} \\ (\theta\alpha_{xx})_{,y} \\ 0 \\ (\theta\alpha_{zz})_{,y} \\ 0 \end{bmatrix}, \quad \boldsymbol{\eta}_\theta^3 = \begin{bmatrix} (\theta\alpha_{zz})_{,z} \\ (\theta\alpha_{xx})_{,z} \\ 0 \\ (\theta\alpha_{yy})_{,z} \\ 0 \end{bmatrix}. \tag{2.13}$$

The symmetric submatrices of the higher-order elastic moduli,

$$\hat{\mathbf{A}}^i = \begin{bmatrix} \hat{a}_{11}^i & \hat{a}_{12}^i & \hat{a}_{13}^i & \hat{a}_{14}^i & \hat{a}_{15}^i \\ & \hat{a}_{22}^i & \hat{a}_{23}^i & \hat{a}_{24}^i & \hat{a}_{25}^i \\ & & \hat{a}_{33}^i & \hat{a}_{34}^i & \hat{a}_{35}^i \\ & & & \hat{a}_{44}^i & \hat{a}_{45}^i \\ & & & & \hat{a}_{55}^i \end{bmatrix}, \quad \hat{\mathbf{A}}^4 = \begin{bmatrix} \hat{a}_{11}^4 & \hat{a}_{12}^4 & \hat{a}_{13}^4 \\ & \hat{a}_{22}^4 & \hat{a}_{23}^4 \\ & & \hat{a}_{33}^4 \end{bmatrix}, \tag{2.14}$$

contain, respectively, fifteen (15), for each $i = 1, 2, 3$, and six (6) independent elastic moduli with units of force.

3. Thermoelastic strain gradient Reissner–Mindlin plate model

This section starts with a derivation for a dimensionally reduced Reissner–Mindlin plate model within the theory of the previous section, followed by the corresponding variational formulation and its discretization. Finally, the plate model is further reduced by proposing a set of constitutive assumptions (with a discussion on the propriety of these assumptions).

3.1. Dimension reduction

A plate structure is assumed to occupy a three-dimensional domain

$$\mathcal{B} = \Omega \times (-\frac{t}{2}, \frac{t}{2}), \tag{3.1}$$

where $\Omega \subset \mathbb{R}^2$ denotes the midsurface of the plate and t stands for the thickness of the plate in the z-direction. For simplicity, the thickness is assumed to be constant. By adopting the classical kinematical Reissner–Mindlin assumptions, the components of the displacement field appear in the form

$$u_x = -z\beta_x(x, y), \quad u_y = -z\beta_y(x, y), \quad u_z = w(x, y), \tag{3.2}$$

where $w : \Omega \to \mathbb{R}$ and $\boldsymbol{\beta} = (\beta_x, \beta_y) : \Omega \to \mathbb{R}^2$, representing the transverse deflection of the midsurface and the rotation vector, respectively, with β_x and β_y being, accordingly, rotations around the y- and x-axes, serve as the independent unknowns of the problem, as in the classical elasticity theory for Reissner–Mindlin plates.

By applying the plane stress assumption $\sigma_{zz} = 0$ and by utilizing the kinematical relations (2.2) and (3.2), the constitutive equations (2.7) take the standard form of the Reissner–Mindlin plate model:

$$\begin{bmatrix} \boldsymbol{\sigma}^1 \\ \boldsymbol{\sigma}^2 \end{bmatrix} = \begin{bmatrix} \mathbf{C}^1 & \mathbf{0} \\ \mathbf{0} & \mathbf{C}^2 \end{bmatrix} \begin{bmatrix} -z\boldsymbol{k} - \boldsymbol{\varepsilon}^\theta \\ \boldsymbol{\gamma} - \mathbf{0} \end{bmatrix}, \tag{3.3}$$

where

$$\boldsymbol{\sigma}^1 = \begin{bmatrix} \sigma_{xx} \\ \sigma_{yy} \\ \sigma_{xy} \end{bmatrix}, \quad \mathbf{C}^1 = \begin{bmatrix} C_{11} & C_{12} & 0 \\ C_{12} & C_{22} & 0 \\ 0 & 0 & C_{66} \end{bmatrix}, \quad \boldsymbol{k} = \begin{bmatrix} \beta_{x,x} \\ \beta_{y,y} \\ \beta_{x,y} + \beta_{y,x} \end{bmatrix}, \tag{3.4}$$

$$\boldsymbol{\sigma}^2 = \begin{bmatrix} \sigma_{yz} \\ \sigma_{xz} \end{bmatrix}, \; \mathbf{C}^2 = \begin{bmatrix} C_{44} & 0 \\ 0 & C_{55} \end{bmatrix}, \; \boldsymbol{\gamma} = \begin{bmatrix} w_{,y} - \beta_y \\ w_{,x} - \beta_x \end{bmatrix}, \; \boldsymbol{\varepsilon}^\theta = \theta \begin{bmatrix} \alpha_{xx} \\ \alpha_{yy} \\ 0 \end{bmatrix}. \tag{3.5}$$

It should be noted that $\mathbf{C}^1$ now corresponds to a plane stress state and $\mathbf{C}^2$ includes the so-called shear correction factor, as detailed in Appendix A.

For double stresses, we adopt assumptions $\mu_{zzx} = \mu_{zzy} = \mu_{zzz} = \mu_{xzz} = \mu_{yzz} = 0$ which, with the kinematical relations (2.2) and (3.2), lead to the following representation of the constitutive equations (2.10):

$$\begin{bmatrix} \boldsymbol{\mu}^1 \\ \boldsymbol{\mu}^2 \\ \boldsymbol{\mu}^3 \\ \boldsymbol{\mu}^4 \end{bmatrix} = \begin{bmatrix} \mathbf{A}^1 & \mathbf{0} & \mathbf{0} & \mathbf{0} \\ \mathbf{0} & \mathbf{A}^2 & \mathbf{0} & \mathbf{0} \\ \mathbf{0} & \mathbf{0} & \mathbf{A}^3 & \mathbf{0} \\ \mathbf{0} & \mathbf{0} & \mathbf{0} & \mathbf{A}^4 \end{bmatrix} \begin{bmatrix} -z\boldsymbol{k}^1 - \boldsymbol{\eta}_\theta^1 \\ -z\boldsymbol{k}^2 - \boldsymbol{\eta}_\theta^2 \\ \boldsymbol{k}^3 - \boldsymbol{\eta}_\theta^3 \\ \boldsymbol{k}^4 - \mathbf{0} \end{bmatrix}, \tag{3.6}$$

where the active double stresses are listed as

$$\boldsymbol{\mu}^1 = \begin{bmatrix} \mu_{xxx} \\ \mu_{yyx} \\ \mu_{xyy} \end{bmatrix}, \quad \boldsymbol{\mu}^2 = \begin{bmatrix} \mu_{yyy} \\ \mu_{xxy} \\ \mu_{xyx} \end{bmatrix}, \quad \boldsymbol{\mu}^3 = \begin{bmatrix} \mu_{xxz} \\ \mu_{xzx} \\ \mu_{yyz} \\ \mu_{yzy} \end{bmatrix}, \quad \boldsymbol{\mu}^4 = \begin{bmatrix} \mu_{xyz} \\ \mu_{xzy} \\ \mu_{yzx} \end{bmatrix}. \tag{3.7}$$

The corresponding strain gradient components are written in the form

$$\boldsymbol{k}^1 = \begin{bmatrix} \beta_{x,xx} \\ \beta_{y,xy} \\ \beta_{x,yy} + \beta_{y,xy} \end{bmatrix}, \quad \boldsymbol{k}^2 = \begin{bmatrix} \beta_{y,yy} \\ \beta_{x,xy} \\ \beta_{x,xy} + \beta_{y,xx} \end{bmatrix}, \tag{3.8}$$

$$\boldsymbol{k}^3 = \begin{bmatrix} -\beta_{x,x} \\ w_{,xx} - \beta_{x,x} \\ -\beta_{y,y} \\ w_{,yy} - \beta_{y,y} \end{bmatrix}, \quad \boldsymbol{k}^4 = \begin{bmatrix} -(\beta_{x,y} + \beta_{y,x}) \\ w_{,xy} - \beta_{x,y} \\ w_{,xy} - \beta_{y,x} \end{bmatrix}. \tag{3.9}$$

The higher-order temperature strains are redefined as

$$\boldsymbol{\eta}_\theta^1 = \begin{bmatrix} (\theta\alpha_{xx})_{,x} \\ (\theta\alpha_{yy})_{,x} \\ 0 \end{bmatrix}, \quad \boldsymbol{\eta}_\theta^2 = \begin{bmatrix} (\theta\alpha_{yy})_{,y} \\ (\theta\alpha_{xx})_{,y} \\ 0 \end{bmatrix}, \quad \boldsymbol{\eta}_\theta^3 = \begin{bmatrix} (\theta\alpha_{xx})_{,x} \\ 0 \\ (\theta\alpha_{yy})_{,z} \\ 0 \end{bmatrix}. \tag{3.10}$$

The submatrices of the higher-order elastic moduli take the form

$$\mathbf{A}^i = \begin{bmatrix} a^i_{11} & a^i_{12} & a^i_{13} \\ & a^i_{22} & a^i_{23} \\ & & a^i_{33} \end{bmatrix}, \quad \mathbf{A}^3 = \begin{bmatrix} a^3_{11} & a^3_{12} & a^3_{13} & a^3_{14} \\ & a^3_{22} & a^3_{23} & a^3_{24} \\ & & a^3_{33} & a^3_{34} \\ & & & a^3_{44} \end{bmatrix}, \tag{3.11}$$

where $i = 1, 2, 4$. It should be noted that $\mathbf{A}^1$, $\mathbf{A}^2$ and $\mathbf{A}^3$ now correspond to the plane stress state, whereas $\mathbf{A}^3$ and $\mathbf{A}^4$ include the so-called shear correction factor by an analogy to the classical model. For details, see Appendix B.

It is worth noting that in the Reissner–Mindlin model of plates made of orthotropic materials which originally are described by fifty one (51) higher-order moduli the number of active higher-order elastic constants is decreased to twenty eight (28).

3.2. Variational formulation

The variational, or weak, form based on PVW can be formulated as follows:
Find $(w, \boldsymbol{\beta}) \in \mathcal{W} \times \boldsymbol{\mathcal{V}}$ such that

$$a(w, \boldsymbol{\beta}; \hat{w}, \hat{\boldsymbol{\beta}}) = l(\hat{w}, \hat{\boldsymbol{\beta}}) \quad \forall (\hat{w}, \hat{\boldsymbol{\beta}}) \in \hat{\mathcal{W}} \times \hat{\boldsymbol{\mathcal{V}}}, \tag{3.12}$$

where the bilinear form a: $(\mathcal{W} \times \boldsymbol{\mathcal{V}}) \times (\hat{\mathcal{W}} \times \hat{\boldsymbol{\mathcal{V}}}) \to \mathbb{R}$, with $a(w, \boldsymbol{\beta}; \hat{w}, \hat{\boldsymbol{\beta}}) = a^c(w, \boldsymbol{\beta}; \hat{w}, \hat{\boldsymbol{\beta}}) + a^g(w, \boldsymbol{\beta}; \hat{w}, \hat{\boldsymbol{\beta}})$, and the load functional l: $\hat{\mathcal{W}} \times \hat{\boldsymbol{\mathcal{V}}} \to \mathbb{R}$, respectively, are defined as

$$a^c(w, \boldsymbol{\beta}; \hat{w}, \hat{\boldsymbol{\beta}}) = \int\limits_{\Omega} \left(\boldsymbol{k}^T \boldsymbol{D}^1 \hat{\boldsymbol{k}} + \boldsymbol{\gamma}^T \boldsymbol{D}^2 \hat{\gamma} \right) \mathrm{d}\Omega, \tag{3.13}$$

$$a^g(w, \boldsymbol{\beta}; \hat{w}, \hat{\boldsymbol{\beta}}) = \sum_{i=1}^{4} \int\limits_{\Omega} (\boldsymbol{k}^i)^T \boldsymbol{R}^i \hat{\boldsymbol{k}}^i \mathrm{d}\Omega, \tag{3.14}$$

$$\begin{aligned} l(\hat{w}, \hat{\boldsymbol{\beta}}) = & \int\limits_{\Omega} \left(f \hat{w} + \boldsymbol{m}^T \hat{\boldsymbol{\beta}} \right) \mathrm{d}\Omega + \int\limits_{\Gamma_{N_1}} Q_1 \hat{w} \mathrm{d}S \\ & + \int\limits_{\Gamma_{N_2}} Q_2 \hat{w}_{,n} \mathrm{d}S + \int\limits_{\Gamma_{N_3}} \boldsymbol{M}_1^T \hat{\boldsymbol{\beta}} \mathrm{d}S + \int\limits_{\Gamma_{N_4}} \boldsymbol{M}_2^T \hat{\boldsymbol{\beta}}_{,n} \mathrm{d}S \\ & + \int\limits_{\Omega} \boldsymbol{\sigma}_\theta^T \hat{\boldsymbol{k}} \mathrm{d}\Omega + \sum_{i=1}^{3} \int\limits_{\Omega} (\boldsymbol{\mu}_\theta^i)^T \hat{\boldsymbol{k}}^i \mathrm{d}\Omega, \end{aligned} \tag{3.15}$$

where $\partial\Omega_N = \Gamma_{N_1} \cup \Gamma_{N_2} \cup \Gamma_{N_3} \cup \Gamma_{N_4}$ denotes the Neumann part of the boundary of the problem domain. The trial function spaces are defined as

$$\mathcal{W} = \{ v \in H^2(\Omega) \mid v_{|\Gamma_{D_1}} = w_1, \ v_{,n|\Gamma_{D_2}} = w_2 \}, \tag{3.16}$$

$$\boldsymbol{\mathcal{V}} = \{ \boldsymbol{\eta} \in [H^2(\Omega)]^2 \mid \boldsymbol{\eta}_{|\Gamma_{D_3}} = \boldsymbol{\eta}_1, \ \boldsymbol{\eta}_{,n|\Gamma_{D_4}} = \boldsymbol{\eta}_2 \}, \tag{3.17}$$

with given Dirichlet data w_1, w_2, $\boldsymbol{\eta}_1$, $\boldsymbol{\eta}_2$ and with $\partial\Omega_D = \Gamma_{D_1} \cup \Gamma_{D_2} \cup \Gamma_{D_3} \cup \Gamma_{D_4}$ denoting the Dirichlet part of the boundary, whereas test function spaces $\hat{\mathcal{W}}$ and $\hat{\boldsymbol{\mathcal{V}}}$ consist of H^2 functions satisfying the corresponding homogeneous Dirichlet boundary conditions. It should be noted that all possible wedge forces are omitted (cf. [37, 57]) assuming smooth boundaries.

The bending rigidity matrices introduced in the bilinear forms (3.13) and (3.14) are defined as

$$\{\boldsymbol{D}^1, \boldsymbol{R}^1, \boldsymbol{R}^2\} = \int_{-t/2}^{t/2} z^2\{\boldsymbol{C}^1, \boldsymbol{A}^1, \boldsymbol{A}^2\}\mathrm{d}z,$$
$$\{\boldsymbol{D}^2, \boldsymbol{R}^3, \boldsymbol{R}^4\} = \int_{-t/2}^{t/2} \{\boldsymbol{C}^2, \boldsymbol{A}^3, \boldsymbol{A}^4\}\mathrm{d}z. \tag{3.18}$$

The temperature stress resultants involved in load functional (3.15) are defined as follows ($i = 1, 2$):

$$\boldsymbol{\mu}_\theta^i = -\int_{-t/2}^{t/2} z\boldsymbol{A}^i\boldsymbol{\eta}_\theta^i\mathrm{d}z, \quad \boldsymbol{\mu}_\theta^3 = \int_{-t/2}^{t/2} \boldsymbol{A}^3\boldsymbol{\eta}_\theta^3\mathrm{d}z, \quad \boldsymbol{\sigma}_\theta = -\int_{-t/2}^{t/2} z\boldsymbol{C}^1\boldsymbol{\varepsilon}^\theta\mathrm{d}z. \tag{3.19}$$

It is worth noting that load functional (3.15), being practically the variation of the work done by the external forces (δW_{ext}) in PVW, is composed in a suitable form for fulfilling the PVW equality. In this way, f acts as a distributed bending force, $\boldsymbol{m}$ stands for a vector of distributed bending moments, Q_1 and $\boldsymbol{M}_1$ are, respectively, the ordinary external transverse bending force and the vector of bending moments, Q_2 and $\boldsymbol{M}_2$ denote the higher-order external loads.

3.3. Conforming isogeometric Galerkin method

A discrete counterpart of problem (3.12) for finding approximate numerical solutions reads as follows:
Find $(w_h, \boldsymbol{\beta}_h) \in \mathcal{W}_h \times \boldsymbol{\mathcal{V}}_h \subset \mathcal{W} \times \boldsymbol{\mathcal{V}}$ such that

$$a(w_h, \boldsymbol{\beta}_h; \hat{w}, \hat{\boldsymbol{\beta}}) = l(\hat{w}, \hat{\boldsymbol{\beta}}) \quad \forall(\hat{w}, \hat{\boldsymbol{\beta}}) \in \hat{\mathcal{W}}_h \times \hat{\boldsymbol{\mathcal{V}}}_h \subset \hat{\mathcal{W}} \times \hat{\boldsymbol{\mathcal{V}}}. \tag{3.20}$$

In isogeometric analysis (IGA), for an isogeometric tensor product discretization of a 2D solution domain, first, a geometrical mapping between the 2D parameter space $[0, 1]^2$ and the plane domain Ω is defined by $\boldsymbol{x} : [0, 1]^2 \to \Omega$ as

$$\boldsymbol{x}(\xi, \eta) = \sum_{i=1}^{n_\xi}\sum_{j=1}^{m_\eta} R_{i,j}^{p,q}(\xi, \eta)\boldsymbol{X}_{i,j}. \tag{3.21}$$

Above, $\boldsymbol{X}_{i,j}$, $i = 1, ..., n_\xi$, $j = 1, ..., m_\eta$, denote the control point (CP) coordinates, while the NURBS basis functions are defined as

$$R_{i,j}^{p,q}(\xi,\eta) = \frac{N_{i,p}(\xi)M_{j,q}(\eta)\omega_{i,j}}{\sum_{\hat{i}=1}^{n}\sum_{\hat{j}=1}^{m} N_{\hat{i},p}(\xi)M_{\hat{j},q}(\eta)\omega_{\hat{i},\hat{j}}}, \tag{3.22}$$

with ξ and η denoting the coordinates of the parameter space. The B-spline basis functions $N_{i,p}$ and $M_{j,q}$ of order p and q, respectively, associated to the open knot vectors $\Xi = \{0 = \xi_1, \xi_2, ..., \xi_{n_\xi+p+1} = 1\}$ and $H = \{0 = \eta_1, \eta_2, ..., \eta_{m_\eta+q+1} = 1\}$, respectively, are defined as follows [78]:

$$N_{i,0}(\xi) = \begin{cases} 1, & \xi_i \leq \xi < \xi_{i+1}, \\ 0, & \text{otherwise} \end{cases} \tag{3.23}$$

$$N_{i,p}(\xi) = \frac{\xi - \xi_i}{\xi_{i+p} - \xi_i} N_{i,p-1}(\xi) + \frac{\xi_{i+p+1} - \xi}{\xi_{i+p+1} - \xi_{i+1}} N_{i+1,p-1}(\xi). \tag{3.24}$$

The corresponding isoparametric discrete space for the approximation of, respectively, the deflection and rotation vector fields

$$w_h(\xi,\eta) = \sum_{i=1}^{n_\xi}\sum_{j=1}^{m_\eta} R_{i,j}^{p,q}(\xi,\eta)W_{i,j}, \quad \boldsymbol{\beta}_h(\xi,\eta) = \sum_{i=1}^{n_\xi}\sum_{j=1}^{m_\eta} R_{i,j}^{p,q}(\xi,\eta)\boldsymbol{B}_{i,j} \tag{3.25}$$

is defined such that $w_h \in S_h$ and $\boldsymbol{\beta}_h \in [S_h]^2$ with unknown control variables $W_{i,j}$ and $\boldsymbol{B}_{i,j}$, where $S_h = \{R_{i,j}^{p,q} \circ \boldsymbol{x}^{-1}\}$.

The tensor product mesh of the isogeometric NURBS discretization of the plane surface is defined as (see [63, 64, 58])

$$\mathcal{T}_h = \{K = \boldsymbol{x}([\hat{\xi}_i, \hat{\xi}_{i+1}] \times [\hat{\eta}_j, \hat{\eta}_{j+1}]) \mid 1 \leq i \leq n_p - 1, 1 \leq j \leq n_q - 1\},$$

where $\hat{\Xi} = \{0 = \hat{\xi}_1, ..., \hat{\xi}_{n_p} = 1\}$ and $\hat{H} = \{0 = \hat{\eta}_1, ..., \hat{\eta}_{n_q} = 1\}$ are the modified knot vectors containing the non-repeated knot values of Ξ and H, respectively, with n_p and n_q denoting the number of knots without repetition in the respective directions. The mesh size $h = \max_{K\in\mathcal{T}_h} h_K$ serves as the mesh index, as usual, with $h_K = \text{diam}(K)$.

By assuming global regularity C^{r-1} ($r = \min(p, q)$) over $\mathcal{T}_h$, with $r \geq 2$, it holds that $S_h \subset H^2(\Omega)$, which provides the conformity and consistency of the discrete formulation of (3.20) with $\mathcal{W}_h = S_h \cap \mathcal{W}$, $\hat{\mathcal{W}}_h = S_h \cap \hat{\mathcal{W}}$, and $\boldsymbol{\mathcal{V}}_h = [S_h]^2 \cap \boldsymbol{\mathcal{V}}$, $\hat{\boldsymbol{\mathcal{V}}}_h = [S_h]^2 \cap \hat{\boldsymbol{\mathcal{V}}}$.

It is worth noting that the Galerkin methods for the Reissner–Mindlin plate problem formulated in (3.12) suffer from the numerical shear locking effect for small values of thickness (see details in [79, 60]). Nevertheless, in the current work, the numerical shear locking effect is suppressed by adopting higher-order NURBS functions.

3.4. Constitutively reduced thermoelastic Reissner–Mindlin plate model

In practical applications, at least in static regimes, we assume that in-plane gradients of strains can be neglected, i.e., $\boldsymbol{k}^1 = \boldsymbol{k}^2 = \mathbf{0}$ and $\gamma_{xz,x} = \gamma_{xz,y} = \gamma_{yz,x} = \gamma_{yz,y} = 0$. In particular, dropping these terms reduces the differential order of the problem and the higher-order boundary conditions, accordingly. The validity of such assumptions has been approved in [25, 29] and will be demonstrated in the present work as well. It has been shown as well (see [63, 64, 58, 31, 60, 62]) that the higher-order terms are responsible for boundary layer effects arising in case of non-classical boundary conditions which are not in the scope of this work. Thus, the reduced constitutive law for the double stresses takes the form

$$\boldsymbol{\mu}^R = \mathbf{A}^R(\boldsymbol{k}^R - \boldsymbol{\eta}_\theta^R), \tag{3.26}$$

$$\boldsymbol{\mu}^R = \begin{bmatrix} \mu_{xxz} \\ \mu_{yyz} \\ \mu_{xyz} \end{bmatrix}, \quad \mathbf{A}^R = \begin{bmatrix} a_{11}^3 & a_{13}^3 & 0 \\ & a_{33}^3 & 0 \\ & & a_{11}^4 \end{bmatrix}, \quad \boldsymbol{\eta}_\theta^R = \begin{bmatrix} (\theta\alpha_{xx})_{,z} \\ (\theta\alpha_{yy})_{,z} \\ 0 \end{bmatrix}, \quad \boldsymbol{k}^R = -\boldsymbol{k}. \tag{3.27}$$

It is important to emphasize that the reduced stiffness matrix $\mathbf{A}^R$ is composed of four independent higher-order elastic moduli, coming from submatrices $\mathbf{A}^3$ and $\mathbf{A}^4$, which are responsible for size dependency arising in plate bending.

The variational, or weak, formulation of the reduced Reissner–Mindlin plate problem reads as follows: find $(w, \boldsymbol{\beta}) \in \mathcal{W} \times \boldsymbol{\mathcal{V}}$ such that

$$a(w, \boldsymbol{\beta}; \hat{w}, \hat{\boldsymbol{\beta}}) = l(\hat{w}, \hat{\boldsymbol{\beta}}) \quad \forall (\hat{w}, \hat{\boldsymbol{\beta}}) \in \hat{\mathcal{W}} \times \hat{\boldsymbol{\mathcal{V}}}, \tag{3.28}$$

where the bilinear form a: $(\mathcal{W} \times \boldsymbol{\mathcal{V}}) \times (\hat{\mathcal{W}} \times \hat{\boldsymbol{\mathcal{V}}}) \to \mathbb{R}$ and the load functional

l: $\hat{\mathcal{W}} \times \hat{\boldsymbol{\mathcal{V}}} \to \mathbb{R}$, respectively, are defined as

$$a(w, \boldsymbol{\beta}; \hat{w}, \hat{\boldsymbol{\beta}}) = \int_\Omega \left(\boldsymbol{k}^T(\boldsymbol{D}^1 + \boldsymbol{R})\hat{\boldsymbol{k}} + \boldsymbol{\gamma}^T \boldsymbol{D}^2 \hat{\gamma}\right) \mathrm{d}\Omega, \tag{3.29}$$

$$l(\hat{w}, \hat{\boldsymbol{\beta}}) = \int_\Omega \left(f\hat{w} + \boldsymbol{m}^T \hat{\boldsymbol{\beta}}\right) \mathrm{d}\Omega + \int_{\Gamma_{N_1}} Q_1 \hat{w} \mathrm{d}S + \int_{\Gamma_{N_2}} \boldsymbol{M}_1^T \hat{\boldsymbol{\beta}} \mathrm{d}S$$
$$+ \int_\Omega \boldsymbol{\sigma}_\theta^T \hat{\boldsymbol{k}} \mathrm{d}\Omega - \int_\Omega (\boldsymbol{\mu}_\theta^R)^T \hat{\boldsymbol{k}} \mathrm{d}\Omega, \tag{3.30}$$

where

$$\boldsymbol{R} = \int_{-t/2}^{t/2} \boldsymbol{A}^R \mathrm{d}z, \quad \boldsymbol{\mu}_\theta^R = \int_{-t/2}^{t/2} \boldsymbol{A}^R \boldsymbol{\eta}_\theta^R \mathrm{d}z. \tag{3.31}$$

The Neumann part of the boundary is defined as $\partial\Omega_N = \Gamma_{N_1} \cup \Gamma_{N_2}$.

The trial function spaces are defined as

$$\mathcal{W} = \{v \in H^1(\Omega) \mid v_{|\Gamma_{D_1}} = w_1\}, \tag{3.32}$$
$$\boldsymbol{\mathcal{V}} = \{\boldsymbol{\eta} \in [H^1(\Omega)]^2 \mid \boldsymbol{\eta}_{|\Gamma_{D_2}} = \boldsymbol{\eta}_1\}, \tag{3.33}$$

with given Dirichlet data w_1, $\boldsymbol{\eta}_1$ and with $\partial\Omega_D = \Gamma_{D_1} \cup \Gamma_{D_2}$ denoting the Dirichlet part of the boundary, whereas test function spaces $\hat{\mathcal{W}}$ and $\hat{\boldsymbol{\mathcal{V}}}$ consist of H^1 functions satisfying the corresponding homogeneous Dirichlet boundary conditions.

A conforming Galerkin formulation of the reduced Reissner–Mindlin plate problem (3.34) reads as follows: find $(w_h, \boldsymbol{\beta}_h) \in \mathcal{W}_h \times \boldsymbol{\mathcal{V}}_h \subset \mathcal{W} \times \boldsymbol{\mathcal{V}}$ such that

$$a(w_h, \boldsymbol{\beta}_h; \hat{w}, \hat{\boldsymbol{\beta}}) = l(\hat{w}, \hat{\boldsymbol{\beta}}) \quad \forall(\hat{w}, \hat{\boldsymbol{\beta}}) \in \hat{\mathcal{W}}_h \times \hat{\boldsymbol{\mathcal{V}}}_h \subset \hat{\mathcal{W}} \times \hat{\boldsymbol{\mathcal{V}}}. \tag{3.34}$$

By assuming global regularity C^{r-1} ($r = \min(p, q)$) over $\mathcal{T}_h$, with $r \geq 1$, it holds that $S_h \subset H^1(\Omega)$, which provides the conformity and consistency of the discrete formulation of (3.34).

It should be noted that the mechanical terms of the loading functional in formulation (3.28) for the constitutively reduced thermoelastic Reissner–Mindlin plate model are the same as within the classical plate model. This leads to a strong formulation which is formally identical to its classical counterpart (see Appendix C for a simple example).

4. Thermoelastic strain gradient Kirchhoff plate model

This section starts with a derivation for a dimensionally reduced Kirchhoff plate model within the theory of Section 2, followed by the corresponding variational formulation and its discretization. Finally, the plate model is further reduced by proposing a set of constitutive assumptions.

4.1. Dimension reduction

By adopting the classical kinematical assumptions of the Kirchhoff plate model, the components of the displacement field take the form

$$u_x = -zw_{,x}(x,y), \quad u_y = -zw_{,y}(x,y), \quad u_z = w(x,y), \tag{4.1}$$

where $w : \Omega \to \mathbb{R}$ representing the transverse deflection of the midsurface serves as the only independent unknown of the problem, as in the classical elasticity theory for Kirchhoff plates.

By applying plane stress assumptions $\sigma_{zz} = \sigma_{xz} = \sigma_{yz} = 0$ and by utilizing the kinematical relations (2.2) and (4.1), the constitutive equations (2.7) take the standard form of the Kirchhoff plate model:

$$\boldsymbol{\sigma}^1 = \mathbf{C}^1(-z\boldsymbol{k} - \boldsymbol{\varepsilon}^\theta), \tag{4.2}$$

where

$$\boldsymbol{\sigma}^1 = \begin{bmatrix} \sigma_{xx} \\ \sigma_{yy} \\ \sigma_{xy} \end{bmatrix}, \; \mathbf{C}^1 = \begin{bmatrix} C_{11} & C_{12} & 0 \\ C_{12} & C_{22} & 0 \\ 0 & 0 & C_{66} \end{bmatrix}, \; \boldsymbol{k} = \begin{bmatrix} w_{,xx} \\ w_{,yy} \\ 2w_{,xy} \end{bmatrix}, \; \boldsymbol{\varepsilon}^\theta = \theta \begin{bmatrix} \alpha_{xx} \\ \alpha_{yy} \\ 0 \end{bmatrix}. \tag{4.3}$$

As for the Reissner–Mindlin plate model in Section 3, $\mathbf{C}^1$ corresponds to the plane stress state.

For double stresses, by utilizing the kinematical relations (2.2) and (4.1) and by adopting the same assumptions as in Section 3, i.e., $\mu_{zzx} = \mu_{zzy} = \mu_{zzz} = \mu_{xzz} = \mu_{yzz} = 0$, the constitutive relations (2.10) acting in the energy take the form

$$\begin{bmatrix} \boldsymbol{\mu}^1 \\ \boldsymbol{\mu}^2 \\ \boldsymbol{\mu}^3 \\ \boldsymbol{\mu}^4 \end{bmatrix} = \begin{bmatrix} \mathbf{A}^1 & \mathbf{0} & \mathbf{0} & \mathbf{0} \\ \mathbf{0} & \mathbf{A}^2 & \mathbf{0} & \mathbf{0} \\ \mathbf{0} & \mathbf{0} & \mathbf{A}^3 & \mathbf{0} \\ \mathbf{0} & \mathbf{0} & \mathbf{0} & \mathbf{A}^4 \end{bmatrix} \begin{bmatrix} -z\boldsymbol{k}^1 - \boldsymbol{\eta}_\theta^1 \\ -z\boldsymbol{k}^2 - \boldsymbol{\eta}_\theta^2 \\ -\boldsymbol{k}^3 - \boldsymbol{\eta}_\theta^3 \\ -\boldsymbol{k}^4 - \mathbf{0} \end{bmatrix}, \tag{4.4}$$

where

$$\boldsymbol{\mu}^1 = \begin{bmatrix} \mu_{xxx} \\ \mu_{yyx} \\ \mu_{xyy} \end{bmatrix}, \quad \boldsymbol{\mu}^2 = \begin{bmatrix} \mu_{yyy} \\ \mu_{xxy} \\ \mu_{xyx} \end{bmatrix}, \quad \boldsymbol{\mu}^3 = \begin{bmatrix} \mu_{xxz} \\ \mu_{yyz} \end{bmatrix}, \quad \boldsymbol{\mu}^4 = \begin{bmatrix} \mu_{xyz} \end{bmatrix}, \tag{4.5}$$

$$\boldsymbol{k}^1 = \begin{bmatrix} w_{,xxx} \\ w_{,xyy} \\ 2w_{,xyy} \end{bmatrix}, \quad \boldsymbol{k}^2 = \begin{bmatrix} w_{,yyy} \\ w_{,xxy} \\ 2w_{,xxy} \end{bmatrix}, \quad \boldsymbol{k}^3 = \begin{bmatrix} w_{,xx} \\ w_{,yy} \end{bmatrix}, \quad \boldsymbol{k}^4 = \begin{bmatrix} 2w_{,xy} \end{bmatrix}, \tag{4.6}$$

$$\boldsymbol{\eta}_\theta^1 = \begin{bmatrix} (\theta\alpha_{xx})_{,x} \\ (\theta\alpha_{yy})_{,x} \\ 0 \end{bmatrix}, \quad \boldsymbol{\eta}_\theta^2 = \begin{bmatrix} (\theta\alpha_{yy})_{,y} \\ (\theta\alpha_{xx})_{,y} \\ 0 \end{bmatrix}, \quad \boldsymbol{\eta}_\theta^3 = \begin{bmatrix} (\theta\alpha_{xx})_{,z} \\ (\theta\alpha_{yy})_{,z} \end{bmatrix}. \tag{4.7}$$

The submatrices of higher-order elastic moduli appear for $i = 1, 2$ in the form

$$\mathbf{A}^i = \begin{bmatrix} a_{11}^i & a_{12}^i & a_{13}^i \\ & a_{22}^i & a_{23}^i \\ & & a_{33}^i \end{bmatrix}, \quad \mathbf{A}^3 = \begin{bmatrix} a_{11}^3 & a_{13}^3 \\ & a_{33}^3 \end{bmatrix}, \quad \mathbf{A}^4 = \begin{bmatrix} a_{11}^4 \end{bmatrix}. \tag{4.8}$$

It should be noted that in the Kirchhoff model for plates made of orthotropic materials, described in the three-dimensional framework by fifty one (51) higher-order moduli, the number of active higher-order elastic constants decreases to sixteen (16).

4.2. Variational formulation

The variational, or weak, formulation reads as follows:
Find $w \in \mathcal{W} \subset H^3(\Omega)$ such that

$$a(w, \hat{w}) = l(\hat{w}) \quad \forall \hat{w} \in \hat{\mathcal{W}} \subset H^3(\Omega), \tag{4.9}$$

where the bilinear form a: $\mathcal{W} \times \hat{\mathcal{W}} \to \mathbb{R}$, $a(w, \hat{w}) = a^c(w, \hat{w}) + a^g(w, \hat{w})$, and the load functional l: $\hat{\mathcal{W}} \to \mathbb{R}$, respectively, are defined as

$$a^c(w, \hat{w}) = \int\limits_{\Omega} \boldsymbol{k}^T \boldsymbol{D}^1 \hat{\boldsymbol{k}} \mathrm{d}\Omega, \tag{4.10}$$

$$a^g(w, \hat{w}) = \sum_{i=1}^{4} \int\limits_{\Omega} (\boldsymbol{k}^i)^T \boldsymbol{R}^i \hat{\boldsymbol{k}}^i \mathrm{d}\Omega, \tag{4.11}$$

$$\begin{aligned} l(\hat{w}) = &\int\limits_{\Omega} f \hat{w} \mathrm{d}\Omega + \int\limits_{\Gamma_{N_1}} Q \hat{w} \mathrm{d}S + \int\limits_{\Gamma_{N_2}} M_1 \hat{w}_{,n} \mathrm{d}S + \int\limits_{\Gamma_{N_3}} M_2 \hat{w}_{,nn} \mathrm{d}S \\ &+ \int\limits_{\Omega} \boldsymbol{\sigma}_\theta^T \hat{\boldsymbol{k}} \mathrm{d}\Omega + \sum_{i=1}^{3} \int\limits_{\Omega} (\boldsymbol{\mu}_\theta^i)^T \hat{\boldsymbol{k}}^i \mathrm{d}\Omega, \end{aligned} \tag{4.12}$$

where $\partial\Omega_N = \Gamma_{N_1} \cup \Gamma_{N_2} \cup \Gamma_{N_3}$ denotes the Neumann part of the boundary. The trial function space is defined as

$$\mathcal{W} = \{v \in H^3(\Omega) \mid v_{|\Gamma_{D_1}} = w_1,\ v_{,n|\Gamma_{D_2}} = w_2,\ v_{,nn|\Gamma_{D_3}} = w_3\}, \tag{4.13}$$

with given Dirichlet data w_1, w_2, w_3 and with $\partial\Omega_D = \Gamma_{D_1} \cup \Gamma_{D_2} \cup \Gamma_{D_3}$ denoting the Dirichlet part of the boundary, whereas test function space $\hat{\mathcal{W}}$ consists of H^3 functions satisfying the corresponding homogeneous Dirichlet boundary conditions. For the sake of simplicity, wedge forces are excluded (cf. [37, 57]) by assuming smooth boundaries.

The bending rigidity matrices introduced in the bilinear forms (4.10) and (4.11) are defined as follows:

$$\begin{aligned} \{\boldsymbol{D}^1, \boldsymbol{R}^1, \boldsymbol{R}^2\} &= \int\limits_{-t/2}^{t/2} z^2 \{\boldsymbol{C}^1, \boldsymbol{A}^1, \boldsymbol{A}^2\} \mathrm{d}z, \\ \{\boldsymbol{R}^3, \boldsymbol{R}^4\} &= \int\limits_{-t/2}^{t/2} \{\boldsymbol{A}^3, \boldsymbol{A}^4\} \mathrm{d}z. \end{aligned} \tag{4.14}$$

Temperature stress resultants are defined in the form ($i = 1, 2$)

$$\boldsymbol{\mu}_\theta^i = -\int_{-t/2}^{t/2} z\boldsymbol{A}^i\boldsymbol{\eta}_\theta^i \mathrm{d}z, \quad \boldsymbol{\mu}_\theta^3 = -\int_{-t/2}^{t/2} \boldsymbol{A}^3\boldsymbol{\eta}_\theta^3 \mathrm{d}z, \quad \boldsymbol{\sigma}_\theta = -\int_{-t/2}^{t/2} z\boldsymbol{C}^1\boldsymbol{\varepsilon}^\theta \mathrm{d}z. \tag{4.15}$$

As in Section 3, load functional (4.12) is composed in a suitable form for fulfilling the PVW equality. Thus, f acts as a distributed bending force, Q_1 and M_1 stand, respectively, for the ordinary external transverse bending force and moment, whereas M_2 denotes the higher-order external load.

4.3. Conforming isogeometric Galerkin method

A discrete counterpart of problem (4.9) for finding approximate numerical solutions reads as follows: find $w_h \in \mathcal{W}_h \subset \mathcal{W}$ such that

$$a(w_h, \hat{w}) = l(\hat{w}) \quad \forall \hat{w} \in \hat{\mathcal{W}}_h \subset \hat{\mathcal{W}}. \tag{4.16}$$

By assuming global regularity C^{r-1} (see Subsection 3.3, for details) over $\mathcal{T}_h$, with $r = \min(p, q) \geq 3$, it holds that $S_h \subset H^3(\Omega)$, which provides the conformity and consistency of the discrete formulation of (4.16) with $\mathcal{W}_h = S_h \cap \mathcal{W}$ and $\hat{\mathcal{W}}_h = S_h \cap \hat{\mathcal{W}}$.

4.4. Constitutively reduced thermoelastic Kirchhoff plate model

As in Subsection 3.4, we assume that in-plane gradients of strains can be neglected, i.e., $\boldsymbol{k}^1 = \boldsymbol{k}^2 = \boldsymbol{0}$. The reduced constitutive law for the double stresses appears in the same form as for the reduced Reissner–Mindlin plate model of Subsection 3.4, i.e.,

$$\boldsymbol{\mu}^R = \mathbf{A}^R(-\boldsymbol{k} - \boldsymbol{\eta}_\theta^R), \tag{4.17}$$

$$\boldsymbol{\mu}^R = \begin{bmatrix} \mu_{xxz} \\ \mu_{yyz} \\ \mu_{xyz} \end{bmatrix}, \quad \mathbf{A}^R = \begin{bmatrix} a_{11}^3 & a_{13}^3 & 0 \\ & a_{33}^3 & 0 \\ & & a_{11}^4 \end{bmatrix}, \quad \boldsymbol{\eta}_\theta^R = \begin{bmatrix} (\theta\alpha_{xx})_{,z} \\ (\theta\alpha_{yy})_{,z} \\ 0 \end{bmatrix}, \tag{4.18}$$

where matrix $\mathbf{A}^R$ is practically a combination of matrices $\mathbf{A}^3$ and $\mathbf{A}^4$ of (4.8).

The variational, or weak, formulation reads as follows: find $w \in \mathcal{W} \subset H^2(\Omega)$ such that

$$a(w, \hat{w}) = l(\hat{w}) \quad \forall \hat{w} \in \hat{\mathcal{W}} \subset H^2(\Omega), \tag{4.19}$$

where the bilinear form a: $\mathcal{W} \times \hat{\mathcal{W}} \to \mathbb{R}$ and load functional l: $\hat{\mathcal{W}} \to \mathbb{R}$, respectively, are defined as

$$a(w, \hat{w}) = \int_{\Omega} \boldsymbol{k}^T (\boldsymbol{D}^1 + \boldsymbol{R}) \hat{\boldsymbol{k}} \mathrm{d}\Omega, \tag{4.20}$$

$$l(\hat{w}) = \int_{\Omega} f \hat{w} \mathrm{d}\Omega + \int_{\Gamma_{N_1}} Q \hat{w} \mathrm{d}S + \int_{\Gamma_{N_2}} M_1 \hat{w}_{,n} \mathrm{d}S + \int_{\Omega} \boldsymbol{\sigma}_{\theta}^T \hat{\boldsymbol{k}} \mathrm{d}\Omega - \int_{\Omega} (\boldsymbol{\mu}_{\theta}^R)^T \hat{\boldsymbol{k}} \mathrm{d}\Omega, \tag{4.21}$$

where

$$\boldsymbol{R} = \int_{-t/2}^{t/2} \boldsymbol{A}^R \mathrm{d}z, \quad \boldsymbol{\mu}_{\theta}^R = \int_{-t/2}^{t/2} \boldsymbol{A}^R \boldsymbol{\eta}_{\theta}^R \mathrm{d}z. \tag{4.22}$$

The Neumann part of the boundary is defined as $\partial\Omega_N = \Gamma_{N_1} \cup \Gamma_{N_2}$. The trial function space is defined as

$$\mathcal{W} = \{v \in H^2(\Omega) \mid v_{|\Gamma_{D_1}} = w_1, \; v_{,n|\Gamma_{D_2}} = w_2\}, \tag{4.23}$$

with given Dirichlet data w_1, w_2 and with $\partial\Omega_D = \Gamma_{D_1} \cup \Gamma_{D_2}$ denoting the Dirichlet part of the boundary, whereas test function space $\hat{\mathcal{W}}$ consists of H^2 functions satisfying the corresponding homogeneous Dirichlet boundary conditions.

A conforming Galerkin formulation of the reduced Kirchhoff plate problem (4.19) reads as follows: find $w_h \in \mathcal{W}_h \subset \mathcal{W}$ such that

$$a(w_h, \hat{w}) = l(\hat{w}) \quad \forall \hat{w} \in \hat{\mathcal{W}}_h \subset \hat{\mathcal{W}}. \tag{4.24}$$

By assuming global regularity C^{r-1} ($r = \min(p, q)$) over $\mathcal{T}_h$, with $r \geq 2$, it holds that $S_h \subset H^2(\Omega)$, which provides the conformity and consistency of the discrete formulation of (4.24).

As for the Reissner-Mindlin plate model of Section 3.4, the constitutively reduced thermoelastic Kirchhoff plate model leads to a strong formulation formally identical to its classical counterpart (see Appendix D for an example).

5. Computational homogenization towards classical continuum

In this section, we consider a 3D metamaterial with a cellular microarchitecture obtained from a 2D triangular lattice (lying in the x_1x_3-plane, see Fig. 5.1c) by an extrusion in the out-of-plane direction along the (third) x_2-axis (see Fig. 5.1a and 5.1b). The base (parent) material is assumed to be isotropic with Young's modulus E, Poisson's ratio ν and a linear thermal expansion coefficient α given in Table 1 for three different materials: steel, aluminium and concrete.

Table 1: Base material properties.

Base material	E, [GPa]	ν	α, [10^{-6} K^{-1}]
Steel	200	0.25	12
Aluminium	69	0.32	22
Concrete	30	0.2	14

The effective classical thermomechanical properties are determined according to [75] (see [80, 81] as well). Since the metamaterial of interest possesses a hexagonal symmetry, it is expected to get five independent elastic moduli and two independent coefficients of linear thermal expansion corresponding to transversally isotropic materials. For the effective homogenized continuum, we further utilize the Duhamel–Neumann constitutive law for a bit more general case of orthotropic thermoelastic materials having nine independent elastic moduli and three thermal expansion coefficients.

The representative volume element (RVE) used in the homogenization procedure is depicted in Fig. 5.1. The geometrical characteristics are collected in Table 2.

Table 2: Dimensions of the RVE.

h_1, [mm]	h_2, [mm]	h_3, [mm]	h_4, [mm]	φ, [°]
5	5	8.66	0.5	60

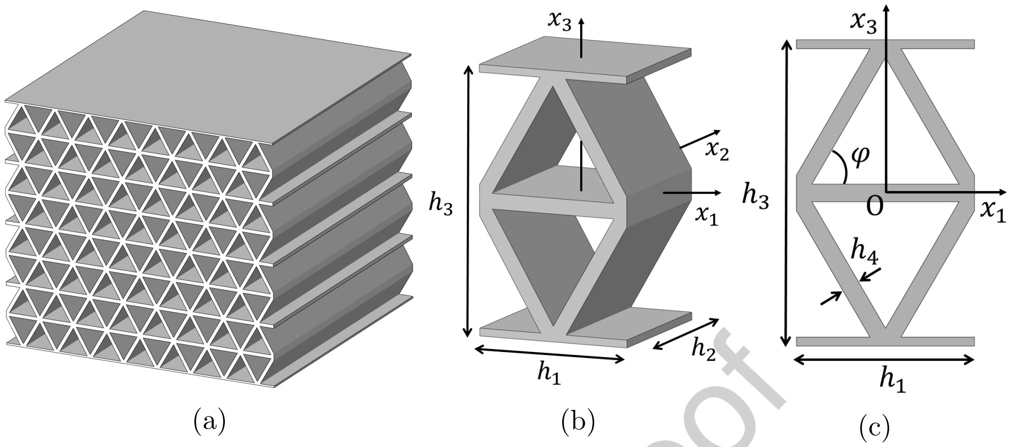

Figure 5.1: Metamaterial of a triangular cellular web (triangular honeycomb) (a), the corresponding 3D RVE (b) and RVE's section in the x_1x_3-plane (c).

For defining the effective elastic moduli, we first solve three problems by stretching the RVE in the directions of axes x_1, x_2 and x_3 (see Fig. 5.1) by setting the following boundary conditions: $u_1 = \pm u_1^\circ/2$ at $x_1 = \pm h_1/2$, $u_2 = 0$ at $x_2 = \pm h_2/2$, $u_3 = 0$ at $x_3 = \pm h_3/2$, for problem (1); $u_2 = \pm u_2^\circ/2$ at $x_2 = \pm h_2/2$, $u_1 = 0$ at $x_1 = \pm h_1/2$, $u_3 = 0$ at $x_3 = \pm h_3/2$, for problem (2); and $u_3 = \pm u_2^\circ/2$ at $x_3 = \pm h_3/2$, $u_1 = 0$ at $x_1 = \pm h_1/2$, $u_2 = 0$ at $x_2 = \pm h_2/2$, for problem (3). Next, for determining shear moduli, we solve three problems by shearing the RVE in the directions of axes x_1, x_2 and x_3 (see Fig. 5.1) by setting the following boundary conditions: $u_1 = 0$ at $x_1 = \pm h_1/2$, $u_3 = \pm u_4^\circ/2$, $u_1 = 0$ at $x_2 = \pm h_2/2$, $u_1 = u_2 = 0$ at $x_3 = \pm h_3/2$, for problem (4); $u_3 = u_2 = 0$ at $x_1 = \pm h_1/2$, $u_2 = 0$ at $x_2 = \pm h_2/2$, $u_1 = \pm u_5^\circ/2$, $u_2 = 0$ at $x_3 = \pm h_3/2$, for problem (5); and $u_2 = \pm u_6^\circ/2$, $u_3 = 0$ at $x_1 = \pm h_1/2$, $u_3 = u_1 = 0$ at $x_2 = \pm h_2/2$, $u_3 = 0$ at $x_3 = \pm h_3/2$, for problem (6).

The effective elastic properties are defined by resolving the equations of the generalized Hooke's law with respect to three Young's moduli, six Poisson's ratios and three shear moduli:

$$\begin{cases} E_1\varepsilon_{11}^\circ\delta_{1i} &= \langle\sigma_{11}^{(i)}\rangle - \nu_{12}\langle\sigma_{22}^{(i)}\rangle - \nu_{13}\langle\sigma_{33}^{(i)}\rangle \\ E_2\varepsilon_{22}^\circ\delta_{2i} &= \langle\sigma_{22}^{(i)}\rangle - \nu_{21}\langle\sigma_{11}^{(i)}\rangle - \nu_{23}\langle\sigma_{33}^{(i)}\rangle \\ E_3\varepsilon_{33}^\circ\delta_{3i} &= \langle\sigma_{33}^{(i)}\rangle - \nu_{31}\langle\sigma_{11}^{(i)}\rangle - \nu_{32}\langle\sigma_{22}^{(i)}\rangle \end{cases}, \quad i = 1, 2, 3 \tag{5.1}$$

$$G_{23}\gamma_{23}^\circ = \langle\sigma_{23}^{(4)}\rangle, \quad G_{13}\gamma_{13}^\circ = \langle\sigma_{13}^{(5)}\rangle, \quad G_{12}\gamma_{12}^\circ = \langle\sigma_{12}^{(6)}\rangle, \tag{5.2}$$

where δ_{ij} denotes the Kronecker delta, $\varepsilon^{\circ}_{jj} = u^{\circ}_j/h_j$ (no summation), $j = 1, 2, 3$, and $\gamma^{\circ}_{23} = u^{\circ}_4/h_2$, $\gamma^{\circ}_{13} = u^{\circ}_5/h_3$, $\gamma^{\circ}_{12} = u^{\circ}_6/h_1$. The Young's moduli and Poisson's ratios are coupled by the following equalities

$$E_1\nu_{21} = E_2\nu_{12}, \quad E_2\nu_{32} = E_3\nu_{23}, \quad E_3\nu_{13} = E_1\nu_{31}. \tag{5.3}$$

The superscripts (i) indicate that the corresponding strains and stresses are defined upon solving problems (i), $i = 1, ..., 6$, respectively. The averaging procedure is defined as

$$\langle \boldsymbol{\sigma} \rangle = \frac{1}{V}\int\limits_V \boldsymbol{\sigma} dV, \tag{5.4}$$

where $V = h_1h_2h_3$ denotes the RVE volume.

The values of the effective elastic constants are listed in Tables 3 and 4. It should be noted that requirements (5.3) are fulfilled.

Table 3: Classical effective moduli (E_i, $i = 1, 2, 3$, in [GPa]).

Base material	E_1	E_2	E_3	ν_{12}	ν_{21}	ν_{13}	ν_{31}	ν_{23}	ν_{32}
Steel	25.60	63.28	25.60	0.101	0.25	0.312	0.312	0.25	0.101
Aluminium	9.06	21.83	9.06	0.133	0.32	0.305	0.305	0.32	0.133
Concrete	3.79	9.49	3.79	0.08	0.2	0.314	0.314	0.2	0.08

Table 4: Classical effective shear moduli [GPa].

Base material	G_{23}	G_{13}	G_{12}
Steel	14.43	9.76	14.43
Aluminium	4.70	3.47	4.70
Concrete	2.24	1.44	2.24

As can be seen, the following equalities hold true

$$\nu_{12} = \nu_{32}, \quad \nu_{13} = \nu_{31}, \quad \nu_{21} = \nu_{23}, \tag{5.5}$$

$$E_3 = E_1, \quad G_{23} = G_{12}, \quad G_{13} = E_1/2/(1 + \nu_{13}), \tag{5.6}$$

which in combination with requirements (5.3) leaves five independent elastic moduli, as is expected for transversal isotropy.

In terms of the components of stiffness matrices $\hat{\mathbf{C}}^1$ and $\hat{\mathbf{C}}^2$ of (2.7), the elastic properties are given in Table 5, where equalities $\hat{C}_{33} = \hat{C}_{11}$, $\hat{C}_{23} = \hat{C}_{12}$, $\hat{C}_{13} = \hat{C}_{11} - 2\hat{C}_{55}$ and $\hat{C}_{44} = \hat{C}_{66}$ valid for transversally isotropic materials are fulfilled.

Table 5: Classical effective moduli [GPa].

Base material	$\hat{C}_{11}$	$\hat{C}_{12}$	$\hat{C}_{13}$	$\hat{C}_{22}$	$\hat{C}_{23}$	$\hat{C}_{33}$	$\hat{C}_{44}$	$\hat{C}_{55}$	$\hat{C}_{66}$
Steel	29.86	10.05	10.35	68.34	10.05	29.86	14.43	9.76	14.43
Aluminium	10.90	4.75	3.96	24.88	4.75	10.90	4.70	3.47	4.70
Concrete	4.34	1.16	1.46	9.96	1.16	4.34	2.24	1.44	2.24

For defining the effective coefficients of linear thermal expansion, we finally solve a coupled temperature-displacement problem by applying a homogeneous temperature field $\Delta\theta$ to the RVE domain. Boundary conditions prescribed in this case are $u_1 = 0$ at $x_1 = \pm h_1/2$, $u_2 = 0$ at $x_2 = \pm h_2/2$, $u_3 = 0$ at $x_3 = \pm h_3/2$, for problem (7). The effective thermal expansion coefficients (collected in Table 6) are defined by resolving the equations of the Duhamel–Neumann law with respect to three moduli α_1, α_2 and α_3:

$$\alpha_1 = -\frac{1}{\Delta\theta E_1}\big(\langle\sigma_{11}^{(7)}\rangle - \nu_{12}\langle\sigma_{22}^{(7)}\rangle - \nu_{13}\langle\sigma_{33}^{(7)}\rangle\big), \tag{5.7}$$

$$\alpha_2 = -\frac{1}{\Delta\theta E_2}\big(\langle\sigma_{22}^{(7)}\rangle - \nu_{21}\langle\sigma_{11}^{(7)}\rangle - \nu_{23}\langle\sigma_{33}^{(7)}\rangle\big), \tag{5.8}$$

$$\alpha_3 = -\frac{1}{\Delta\theta E_3}\big(\langle\sigma_{33}^{(7)}\rangle - \nu_{31}\langle\sigma_{11}^{(7)}\rangle - \nu_{32}\langle\sigma_{22}^{(7)}\rangle\big), \tag{5.9}$$

where the values of Young's moduli and Poisson's ratios are taken from Table 3.

Table 6: Classical effective coefficients of linear thermal expansion [10^{-6} K^{-1}].

Base material	α_1	α_2	α_3
Steel	12	12	12
Aluminium	22	22	22
Concrete	14	14	14

It should be noted that the values of the effective thermal expansion moduli coincide with each other and with the corresponding value of the base material, i.e., $\alpha_1 = \alpha_2 = \alpha_3 = \alpha$ for each base material.

6. Identification procedure for higher-order moduli

In this section, we propose an identification procedure aiming at determining the higher-order elastic moduli for a cellular plate structure described by an equivalent, anisotropic, higher-order continuum plate model. We investigate plate structures made of the triangular cellular metamaterial of Section 5, with the plate midsurface parallel to the x_1x_2-plane of the RVE. In essence, the identification procedure consists of four different loading cases exiting four different deformation modes for a series of plate structures, and particularly, modeling these deformations with both (i) a full-field (reference) model relying on classical three-dimensional elasticity and (ii) a higher-order plate model based on strain gradient elasticity. Matching the results of these two models identifies the parameters of the higher-order plate model.

In what follows, we alternately define four independent higher-order moduli – a^3_{11}, a^3_{13}, a^3_{33} and a^4_{11} – of the constitutive matrix $\mathbf{A}^R$ of (3.27). The full-field reference solutions for all the loading cases are obtained via the classical finite element method (the FEM software Abaqus), whereas for the results of the reduced strain gradient plate models we use analytical solutions for the first two loading cases of cylindical bending, whereas numerical solutions based on isogeometric analysis (user elements within Abaqus) are used for the last two loading cases of twisting and double curvature bending. It should be emphasized that the series of plate structures for the first two loading cases consist of five plates with different number of microstructural layers, whereas the series for the third load case includes four plates and the fourth load case series includes three plates. In practice, however, when knowing that the model is correct, a pair of plates or even one plate would be enough for matching the higher-order plate model with the reference model and finding the parameter values accordingly.

6.1. Higher-order elastic modulus a^3_{11} – via cylindrical bending

Let us consider rectangular plate structures of length L, thickness t ($t < L$) and width b ($b \gg L$) schematically presented in Fig. 6.1a. The boundary conditions corresponding to clamped and simply supported plates, respectively, are presented in the top and bottom of Fig. 6.1b. Bending is considered to occur in the xz-plane.

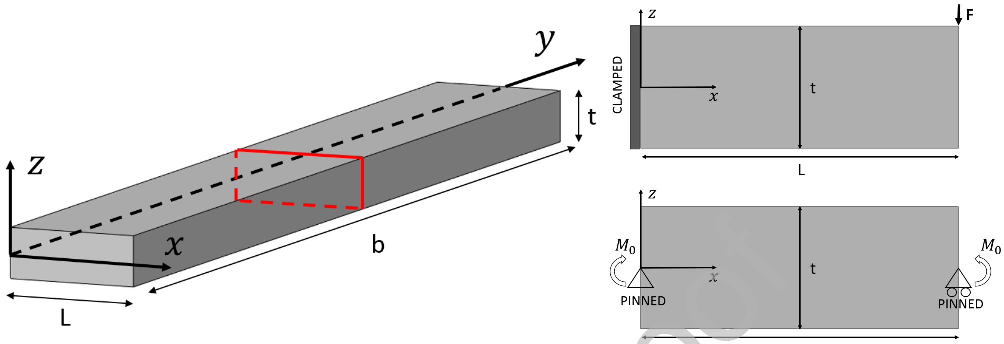

(a) Plate structure.

(b) Boundary conditions.

Figure 6.1: Plate structure representation.

Plates are made of the triangular cellular metamaterial of Section 5 such that the local coordinate axes x_1 and x_2 of the microarchitecture (Fig. 5.1b) coincide, respectively, with the global coordinate axes x and y of the plate. Depending on the number of the triangular layers N in the thickness direction, a series of five plates with $N = 1, 2, 3, 4$ and 8 is constructed such that the L-to-t ratio remains constant: for each plate, $L/t = N(2h_1)/(Nh_3/2) = 2.31$ (see Fig. 6.2 for the samples and Table 2 for the dimensions).

In the simply supported case, the microarchitected plates are pinned along the coordinate lines $x = 0$ and $x = L$ such that the corresponding lateral edges can freely rotate around the y-axis under an applied bending moment M_0 distributed along the boundary. Bending rigidity D in this case is calculated as $D = M_0/(t^2\varphi_L)$, where φ_L denotes the rotation angle at $x = L$. The corresponding analytical expressions (which coincide for simply supported boundary conditions) derived for the reduced Reissner–Mindlin and Kirchhoff strain gradient plate models of Sections 3.4 and 4.4, respectively, are given as (see Appendix C)

$$D_{gr} = \frac{t}{6L}(C_{11} + \frac{12}{t^2}a^3_{11}). \tag{6.1}$$

It is worth noting that from among the four higher-order moduli only a^3_{11} remains active when bending happens in the xz-plane.

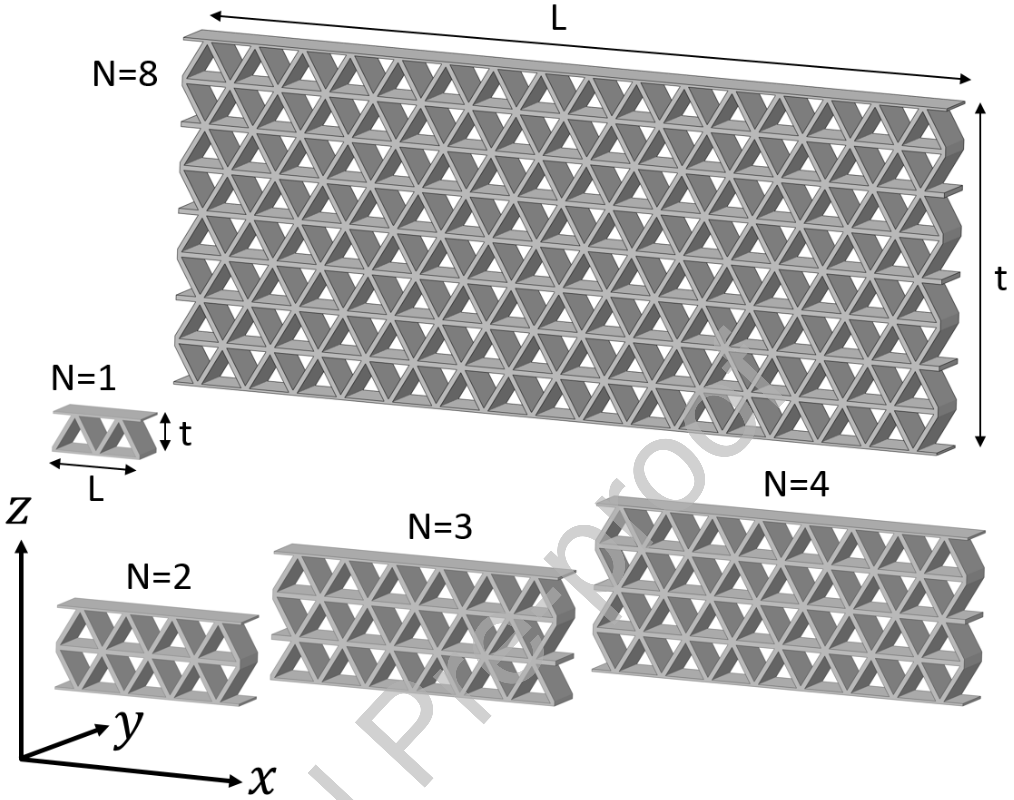

Figure 6.2: Cross-sections of the microarchitected plates schematically represented as the red frame in Fig. 6.1a. The length-to-thickness ratio is kept as $L/t = 2.31$.

The full-field simulation results are shown in Fig. 6.3a and Figs. F.1a and F.2a of Appendix E, as the dependence of bending rigidity on the plate thickness, respectively, for steel, aluminium and concrete as base material. The blue dots relate to the microarchitected plates with $N = 1, 2, 3, 4$ and 8, or $t = 4.33$ mm, 8.66 mm, 12.99 mm, 17.32 mm and 34.64 mm, respectively. The red line corresponds to expression (6.1). The classical C_{11}-modulus through expression (A.2) involves the known values from Table 5 calculated via the computational homogenization presented in Section 5. The higher-order a^3_{11}-modulus is calibrated such that the red line fits to the blue dots. The corresponding values of the modulus are collected in Table 7 for each base material. The black line represents the bending rigidity which remains constant within classical plate theories. The corresponding expression is obtained from (6.1) by dropping the a^3_{11}-modulus. It can be seen that for thin microarchitected plates the classical elasticity model fails to describe the significant size effect, whereas for more than eight layers ($N \geq 8$) the influence of the microarchitecture is negligible and bending predictions based on both classical and gradient elasticity theories almost coincide.

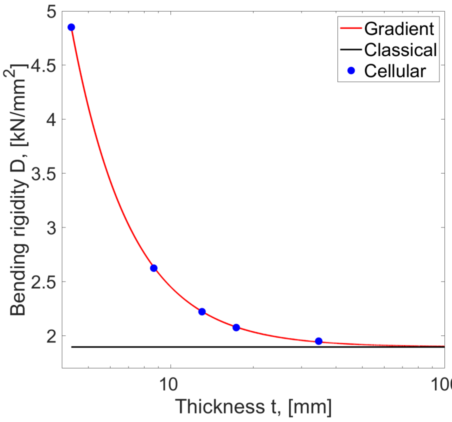

(a) Simply supported case

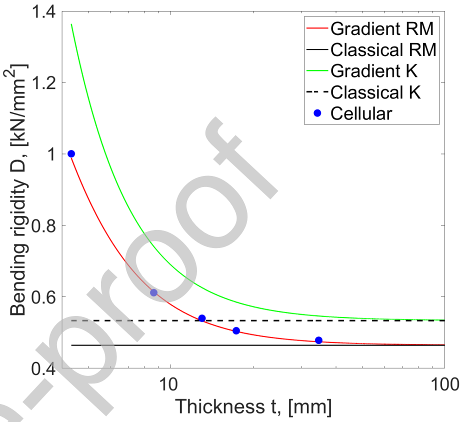

(b) Clamped case

Figure 6.3: Bending rigidity versus plate thickness for steel as base material.

As a double check for the value of modulus a_{11}^3 and in order to demonstrate the difference between the Kirchhoff and Reissner–Mindlin plate models, we study a series of cantilever plates: the microarchitected plates are clamped at $x = 0$, while at $x = L$ the corresponding lateral edges can freely move under an applied transversal force F distributed along the boundary. Bending rigidity D in this case is defined as $D = F/w_L$, where w_L denotes the deflection at $x = L$. The corresponding analytical expression derived for the reduced Reissner–Mindlin strain gradient plate model of Section 3.4 reads as

$$D_{gr} = \frac{t}{L}\frac{(C_{11} + 12a_{11}^3/t^2)C_{55}}{4C_{55}L^2/t^2 + C_{11} + 12a_{11}^3/t^2}. \tag{6.2}$$

For the reduced Kirchhoff strain gradient plate model of Section 4.4, the analytical expression is derived in the form

$$D_{gr} = \frac{t^3}{4L^3}(C_{11} + \frac{12}{t^2}a_{11}^3). \tag{6.3}$$

See Appendices C and D for the derivations.

The full-field simulation results are shown in Fig. 6.3b and Figs. F.1b and F.2b of Appendix E, respectively, for steel, aluminium and concrete as base material. The blue dots relate to the microarchitected plates. The red line corresponds to expression (6.2), while the green one follows expression (6.3). The classical moduli C_{11} and C_{55}, through expressions (A.2) and (A.3), respectively, involve the known values from Table 5 calculated via the computational homogenization of Section 5. The value of a^3_{11}, calibrated previously for the simply supported case, is utilized in expressions (6.2) and (6.3). By analysing these two expressions, it can be seen that equation (6.2) corresponding to the Reissner–Mindlin plate model includes the shear modulus and, hence, adequately captures the full-field simulation results for thick plates. The green line governed by expression (6.3) significantly overestimates the results. Finally, it should be emphasized that in practical cases one prefers to keep the computational costs of reference solutions as low as possible and hence prefers choosing thick (or short) plates; we have shown that the Reissner–Mindlin model is suitable even for very thick plates: now $t/L > 2/5$.

Table 7: Values for modulus a^3_{11}.

Base material	Steel	Aluminium	Concrete
a^3_{11}, [kN]	63.96	23.08	9.36

6.2. *Higher-order elastic modulus a^3_{33} – via cylindrical bending*

In order to determine the higher-order modulus a^3_{33}, the microarchitecture is oriented such that the local coordinate axes x_1 and x_2 of the microarchitecture (Fig. 5.1b) coincide, respectively, with the global coordinate axes y and x of the plate (Fig. 6.1a). As in the previous section, five types of plates with $N = 1, 2, 3, 4$ and 8 are constructed such that the L-to-t ratio is constant and equal to $L/t = 4$, see Fig. 6.4.

For simply supported plates, bending rigidity D is calculated as $D = M_0/(t^2\varphi_L)$, where φ_L denotes the rotation angle at $x = L$. The corresponding analytical expression is given in the form (see Appendix C)

$$D_{gr} = \frac{t}{6L}(C_{22} + \frac{12}{t^2}a^3_{33}). \tag{6.4}$$

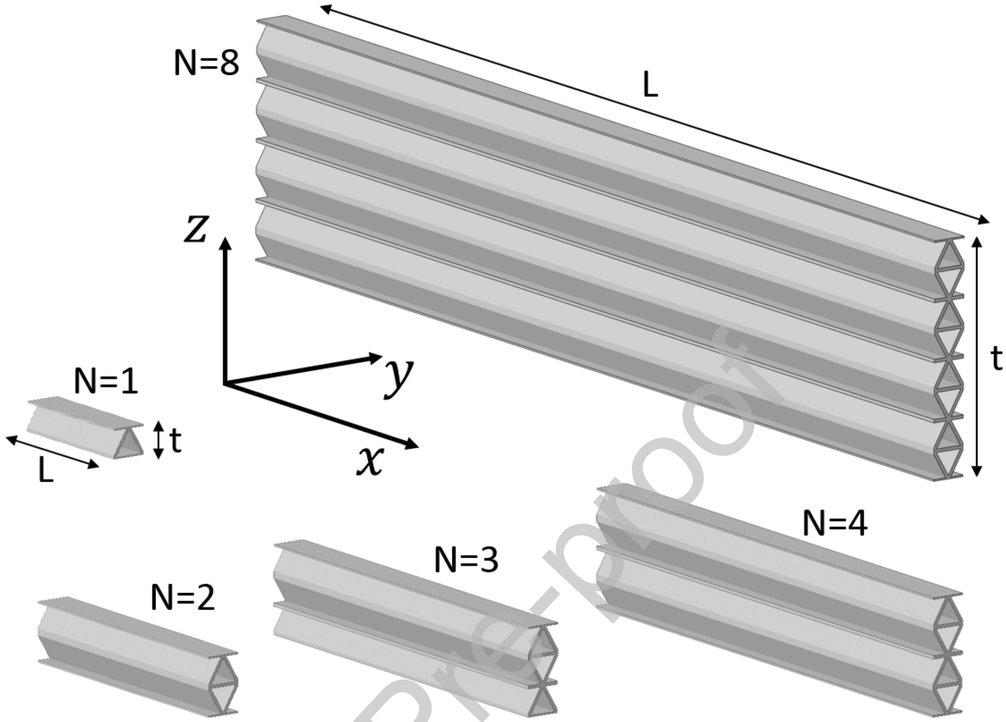

Figure 6.4: Cross-sections of the microarchitected plates schematically represented as the red frame in Fig. 6.1a. Length to thickness ratio is kept as $L/t = 4$.

The full-field simulation results are presented in Fig. 6.5a and Figs. F.3a and F.4a of Appendix F, as the dependence of bending rigidity on the plate thickness, respectively, for steel, aluminium and concrete as base material. The blue dots relate to the microarchitected plates with $N = 1, 2, 3, 4$ and 8, or $t = 4.33$ mm, 8.66 mm, 12.99 mm, 17.32 mm and 34.64 mm, respectively. The red line corresponds to expression (6.4). The classical C_{22}-modulus through expression (A.2) involves the known values from Table 5. The higher-order a^3_{33}-modulus is calibrated such that the red line follows the blue dots. The corresponding values of the modulus are collected in Table 8 for each base material. The black line represents the bending rigidity which remains constant within classical plate theories. The corresponding expression is obtained from (6.4) by setting $a^3_{33} = 0$.

As a double check for the value of modulus a^3_{33} and in order to demonstrate the difference of the Kirchhoff and Reissner–Mindlin plate models, we still study a series of cantilever plates: bending rigidity D is defined as $D = F/w_L$, where w_L denotes the deflection at $x = L$. The corresponding analytical expression derived within the reduced Reissner–Mindlin strain gradient plate model of Section 3.4 reads as (see Appendix C)

$$D_{gr} = \frac{t}{L}\frac{(C_{22} + 12a^3_{33}/t^2)C_{44}}{4C_{44}L^2/t^2 + C_{22} + 12a^3_{33}/t^2}. \tag{6.5}$$

For the reduced Kirchhoff strain gradient plate model of Section 4.4, the analytical expression is defined as (see Appendix D)

$$D_{gr} = \frac{t^3}{4L^3}(C_{22} + \frac{12}{t^2}a^3_{33}). \tag{6.6}$$

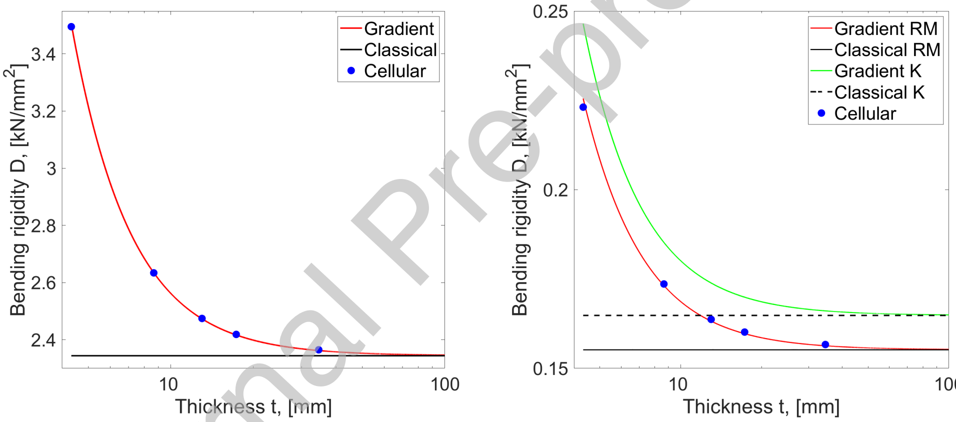

(a) Simply supported case

(b) Clamped case

Figure 6.5: Bending rigidity versus plate thickness for steel as base material.

Table 8: Values for modulus a^3_{33}.

Base material	Steel	Aluminium	Concrete
a^3_{33}, [kN]	50.30	18.27	7.22

The full-field simulation results are shown in Fig. 6.5b and Figs. F.3b and F.4b of Appendix F, respectively, for steel, aluminium and concrete as base material. The blue dots relate to the microarchitected plates. The red line corresponds to expression (6.5), whereas the green one corresponds to expression (6.6). The classical moduli C_{22} and C_{44} of expressions (A.2) and (A.3), respectively, involve the known values from Table 5. The value of a^3_{33}, calibrated previously for the simply supported case, is utilized in expressions (6.5) and (6.6).

6.3. Higher-order elastic modulus a^4_{11} – via twisting

For estimating the a^4_{11}-modulus, we consider twisting of the microarchitected square plates. The global Cartesian coordinate system is placed such that the plate midsurface has $z = 0$ and coordinate axes x and y lie, respectively, along the plate sides AB and BC. The microarchitecture is oriented such that the local coordinate axes x_1 and x_2 of the microarchitecture (Fig. 5.1b) coincide, respectively, with the global coordinate axes x and y of the plate. Four types of microarchitected plates with $N = 1, 2, 3$ and 4, or $t = 4.33$ mm, 8.66 mm, 12.99 mm and 17.32 mm, are constructed such that the ratio of the plate side length L to the plate thickness t is constant and equal to $L/t = 4.62$, see Fig. 6.6. The corner edges of the microarchitected plates are affected by transversal loads with magnitude F leading to plate twisting: upward loadings act at two opposite corners in the ends of one diagonal (A and C in Figure 6.6); downward loadings act at the other two corners (B and D) of the other diagonal. Plate edges parallel to the y-axis are constrained to be rigid.

The microarchitected plates are then modelled by the strain gradient plates of the equivalent homogenized continuum. The twisting problem of the corresponding strain gradient Reissner–Mindlin and Kirchhoff plates is simulated by isogeometric methods implemented in a user element framework of Abaqus [64]. A square domain is discretized by 8×8 finite elements (see Fig. 6.6) with NURBS basis functions of the fifth order resulting in C^4-continuity. The plate corners are subjected to transversal loads with magnitude F. The classical flexural rigidities $\boldsymbol{D}^1$ and $\boldsymbol{D}^2$ of plate problems are defined according to Table 5 via expressions (3.18), (A.2) and (A.3). In the twisting problem, only three of the four higher-order material constants are involved, i.e., the a^3_{13}-modulus remains inactive. The values of the two elastic moduli a^3_{11} and a^3_{33} have been determined in the previous subsections. The a^4_{11}-modulus is now calibrated by the fitting procedure described below. The higher-order flexural rigidity matrix $\boldsymbol{R}$ is calculated by expression from (4.22).

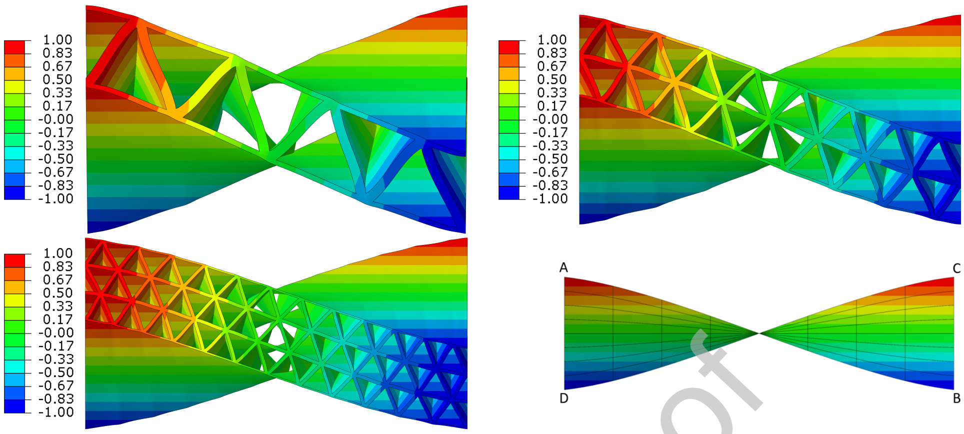

Figure 6.6: Distribution of the normalized (with respect to the deflection of corner C) displacement field on the deformed configuration in the xz-plane for the twisting problem of the microarchitected square plates. The full-field simulation results are presented for $N = 1$ (or $t = 4.33$ mm) in the top left, for $N = 2$ (or $t = 8.66$ mm) in the top right and for $N = 3$ (or $t = 12.99$ mm) in the bottom left positions. The IGA simulation results of the corresponding strain gradient Reissner–Mindlin plate of an equivalent continuum are shown in the bottom right position for $N = 3$. The length-to-thickness ratio is $L/t = 4.62$.

The full-field simulation results for the microarchitected plates as well as the IGA simulations of the corresponding strain gradient plate problems are shown in Fig. 6.7a and Figs. G.1a and G.2a of Appendix G, respectively, for steel, aluminium and concrete as base materials. Bending rigidity in this case is defined as $D = FL/(2t^2 w_C)$, where w_C stands for the transversal deflection of the plate corner. The blue dots relate to the microarchitected plates with $N = 1, 2, 3$ and 4, or $t = 4.33$ mm, 8.66 mm, 12.99 mm and 17.32 mm, respectively. The red line corresponds to the strain gradient Reissner–Mindlin plate model, while the green one relates to the strain gradient Kirchhoff plate model. The simulation results corresponding to the classical plate models are plotted with the straight black lines (solid for the Reissner–Mindlin and dashed for the Kirchhoff models) reflecting the size-independent nature of the classical continuum theories. By varying the plate thickness t and by keeping the ratio of the plate side length to the thickness constant, several hundreds of IGA simulations for both the Reissner–Mindlin and Kirchhoff plate problems have been performed for representing the corresponding bending rigidities by practically continuous curves (looking like plots of analytical curves). The a^4_{11}-modulus is chosen such that the red line fits to the blue dots. Table 9 collects the corresponding parameter values.

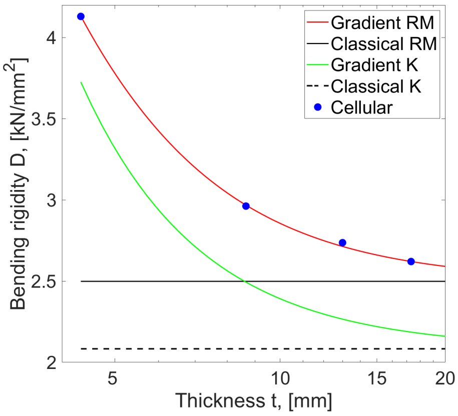

(a) Comparison of plate models.

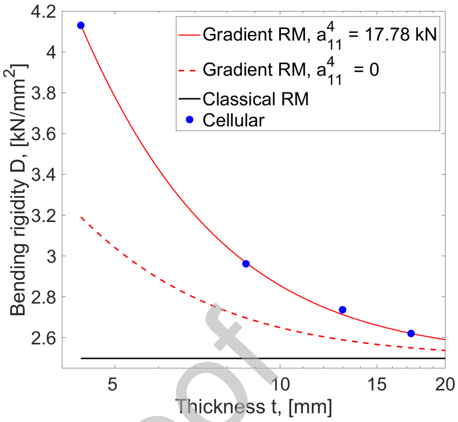

(b) Influence of modulus a^4_{11}.

Figure 6.7: Bending rigidity versus plate thickness for steel as base material.

Fig. 6.7b (see Figs. G.1b and G.2b of Appendix G as well) compares the bending rigidities of the Reissner–Mindlin plate models with the full-field simulation results for the case in which the a^4_{11}-modulus is equal to zero. It can be seen that by neglecting this modulus the plate model significantly underestimates the results, which demonstrates the relevance of this specific modulus.

Table 9: Values for modulus a^4_{11}.

Base material	Steel	Aluminium	Concrete
a^4_{11}, [kN]	17.78	5.57	2.86

6.4. Higher-order elastic modulus a^3_{13} – via double curvature bending

For determining the a^3_{13}-modulus, we consider a right-angled trapezoidal plate under uniformly distributed transversal loading f. The global Cartesian coordinate system is placed such that the plate midsurface has $z = 0$, coordinate axis y lies along the trapezoid bases (sides AD and BC in Fig. 6.8) and axis x is perpendicular to the bases. The microarchitecture is oriented such that the local coordinate axes x_1 and x_2 of the microarchitecture (Fig. 5.1b) coincide, respectively, with the global coordinate axes x and y of the plate. Side AD is simply supported, whereas sides AB and BC are constrained in accordance to symmetry boundary conditions.

Three types of microarchitected plates with $N = 1, 2$ and 3, or $t = 4.33$ mm, 8.66 mm and 12.99 mm, are constructed such that side AD has length $|AD| = L/2$, side AB is of length $|AB| = NL$ and side BC has length $|BC| = (N + 1/2)L$. Length L is set to $L = 20$ mm. It is worth noting that the geometry as well as the loading are selected such that the deformed plate has a saddle shape with double curvature (see Fig. 6.8), i.e., the principal curvatures at point B have opposite signs, which is crucial in order to activate the a^3_{13}-modulus of the equivalent continuum.

The microarchitected plates are modelled by the strain gradient plate models of the equivalent homogenized continuum. For numerical simulations of the corresponding strain gradient Reissner–Mindlin and Kirchhoff plate problems, the trapezoidal domain is discretized by 8×8 finite elements (see Fig. 6.8) with NURBS basis functions of the fifth order with C^4-continuity. In the considered bending problem, all four higher-order material constants are involved. The values of the three elastic moduli a^3_{11}, a^3_{33} and a^4_{11} have been determined in the previous sections. The a^3_{13}-modulus is calibrated by the fitting procedure described below.

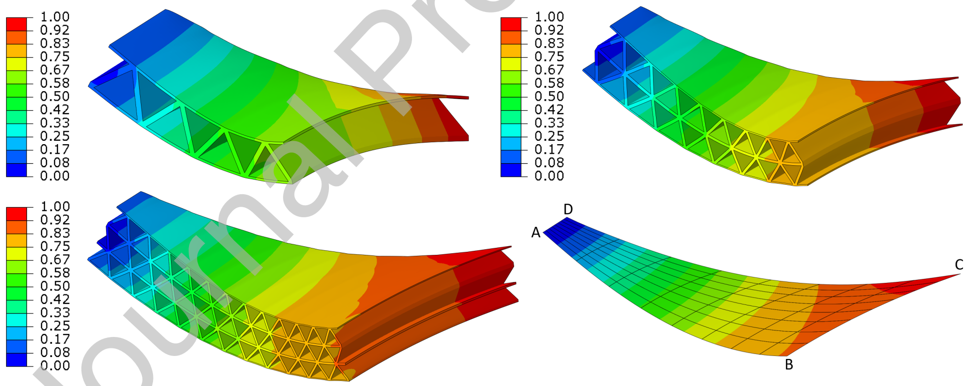

Figure 6.8: The distribution of the normalized (with respect to the deflection of corner C) displacement field in the bending problem of the microarchitected trapezoidal plates. The full-field simulation results are presented for $N = 1$ (or $t = 4.33$ mm) in the top left, for $N = 2$ (or $t = 8.66$ mm) in the top right and for $N = 3$ (or $t = 12.99$ mm) in the bottom left positions. The IGA simulation results of the corresponding strain gradient Reissner–Mindlin plate of an equivalent continuum are shown in the bottom right position for $N = 3$.

The full-field simulation results for the microarchitected plates as well as the IGA simulations of the corresponding strain gradient plate problems are shown in Fig. 6.9a and Figs. H.1a and H.2a of Appendix H, respectively, for steel, aluminium and concrete as base materials. Bending rigidity in this case is defined as a ratio of the distributed load resultant $F = fA_p$ to the transversal deflection of the corner (point C) w_C and the length of side AB, i.e., $D = F/w_C/|AB|$, where A_p denotes the area of the plate domain. The blue dots relate to the microarchitected plates with $N = 1, 2$ and 3 ($t = 4.33$ mm, 8.66 mm and 12.99 mm). The red line corresponds to the strain gradient Reissner–Mindlin plate model, while the green one relates to the strain gradient Kirchhoff plate model. The simulation results corresponding to the classical plate models are plotted as black lines (solid for Reissner–Mindlin and dashed for Kirchhoff). By varying the plate thickness t and keeping the ratio of the plate thickness to the length of side AB constant, several hundreds of IGA simulations for both the Reissner–Mindlin and Kirchhoff plate problems were performed for representing the corresponding bending rigidities by practically continuous curves. The a^3_{13}-modulus is chosen such that the red line fits to the blue dots. The corresponding parameter values are collected in Table 10.

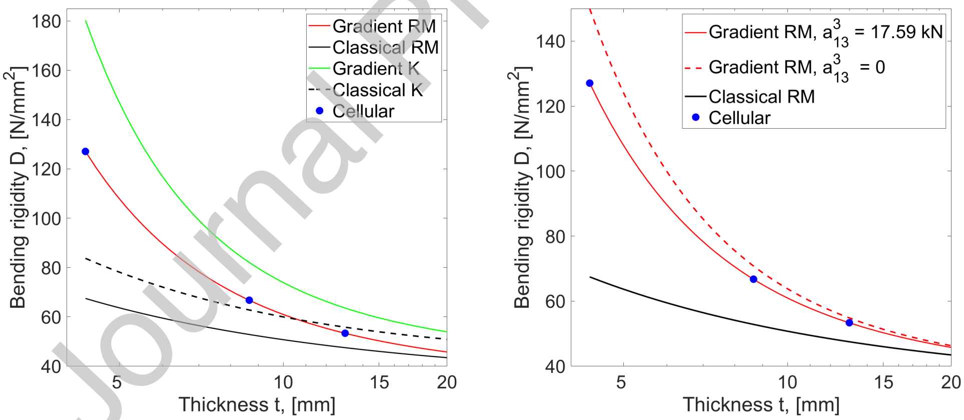

(a) Comparison of plate models. (b) Influence of modulus a^3_{13}.

Figure 6.9: Bending rigidity versus plate thickness for steel as base material.

Fig. 6.9b (see Figs. H.1b and H.2b of Appendix H as well) compares the bending rigidities of the Reissner–Mindlin plate models with the full-field simulation results for the case in which the a^3_{13}-modulus is omitted. It can be seen that by neglecting this modulus the plate model definitely overestimates the results, which demonstrates the relevance of this specific modulus.

Table 10: Values for modulus a^3_{13}.

Base material	Steel	Aluminium	Concrete
a^3_{13}, [kN]	17.59	7.80	2.06

6.5. Explicit representation of length scale parameters

The non-classical elastic moduli identified (or calibrated) in Sections 6.1, 6.2, 6.3 and 6.4 are collected below in Table 11. In the table, we use the components of matrix $\mathbf{A}^R$ of the plate model defined as $A^R_{11} = a^3_{11}$, $A^R_{22} = a^3_{33}$, $A^R_{33} = a^4_{11}$, $A^R_{12} = a^3_{13}$.

Table 11: Higher-order moduli A^R_{ij} [kN].

Base material	A^R_{11}	A^R_{22}	A^R_{33}	A^R_{12}
Steel	63.96	50.30	17.78	17.59
Aluminium	23.08	18.27	5.57	7.80
Concrete	9.36	7.22	2.86	2.06

In order to further study the character of these values, we write down the following relation (inspired by and to be compared to the so-called weak nonlocality assumption $A_{ijklmn} = L_{kn}C_{ijlm}$ [69, 71]) between the higher-order material parameters (3.27) and the classical elastic moduli (3.4) of the plate model:

$$A^R_{ij} = g^2_{ij}C^1_{ij}. \tag{6.7}$$

This relation (no summation on indices i, j) introduces four independent length scale parameters g_{ij} listed in Table 12.

Table 12: Length scale parameters g_{ij} [mm].

Base material	g_{11}	g_{22}	g_{33}	g_{12}
Steel	1.56	0.880	1.11	1.64
Aluminium	1.56	0.895	1.09	1.61
Concrete	1.56	0.865	1.13	1.64

First, as can be seen in the table the values of the length scale parameters are comparable to the characteristic length scale of the microarchitecture, i.e., width h_1 or half height $h_3/2$ of the RVE (see Fig. 5.1 and Table 2). It is worth noting that for different base materials, the values of the length scale constants of the cellular metamaterial almost coincide approving the fact that the length scale parameters depend mainly on the geometry of the microarchitecture. Since the classical material moduli of the equivalent continuum are nonlinearly dependent on Poisson's ratio of the base material, the values of the particular length scale parameter are not identical.

Second, we note that although equation (6.7) formally resembles the assumption of the so-called weak nonlocality [69, 71] it is quite clear that assumption cannot be used as a starting point for our analysis: for transversal isotropy, weak nonlocality implies only two independent length scale parameters, whereas by starting from the general form of strain gradient elasticity we have arrived at four parameters – even after some constitutive model reductions concerning the gradient terms (see Sections 3.4 and 4.4). And each of these parameters has shown to have a crucial role in modeling the different deformations modes of plate bending.

7. Examples

This section briefly lists some examples demonstrating that after the homogenization has been accomplished for the chosen microarchitecture, the plate model can be used for modelling microarchitectural plates of any geometry or number of layers (with classical transversally isotropic (meta)material parameters in matrices $\mathbf{C}^i$ and the reduced set of strain gradient (meta)material parameters in matrices $\mathbf{A}^i$).

We have chosen here the following examples: a square plate, a circular plate, an annular plate. For each example, results for the plate model are presented beside the corresponding references solution, a fine-scale model discretized with three-dimensional solid elements. For the square plate, we consider the case of simultaneously applied mechanical and thermal loads and compare the full-field simulation results with the predictions of the reduced strain gradient and the corresponding classical thermoelastic Reissner–Mindlin plate models. For the circular and annular plates, we separate the mechanically and thermally induced bending cases and demonstrate a fiasco of thermomechanically incomplete plate models (with respect to higher-order constitutive laws) in capturing the bending response.

7.1. Square plate

As the first example, we consider a square plate with rotated microarchitecture (Fig. 7.1 left column) made of isotropic steel with material properties listed in Table 1. The global Cartesian coordinate system is placed such that the plate midsurface has $z = 0$ and coordinate axes x and y lie along the plate sides AB and AD, respectively (see Fig. 7.1). The microarchitecture is oriented such that the local coordinate axis x_3 is parallel to the z-axis (i.e., the x_1x_2-plane and the xy-plane are parallel, see Fig. 5.1b) and the x_1-axis is rotated by an angle of 45° around the z-axis such that the local coordinate axis x_2 is parallel to the plate diagonal BD. Two types of microarchitected plates with $N = 1$ and 2 or $t = 4.33$ mm and 8.66 mm are constructed such that the plate side length L is kept constant ($L = 60$ mm giving moderately thick plates with $t/L \sim 1/10$).

In this example, we consider a plate deformation caused by simultaneously applied mechanical and thermal loads. A uniformly distributed load f with $f/t = 1.24\bar{c}$ N/mm^3 affects a middle patch of the plate in the transversal direction as shown in Fig. 7.1 (bottom right). (A nondimensional scalar $\bar{c}$ ensures that deformations remain small enough for staying in the linear regime; neither yielding for metals nor fracture for concrete should be present.) The patch has dimensions 30 mm × 30 mm. Constant temperatures $+\bar{c}T_0$ and $-\bar{c}T_0$ (with $T_0 = 100$ °C) are prescribed, respectively, at the upper ($z = -t/2$) and lower ($z = t/2$) plate surfaces. Sides AB and AD are fully clamped. The rest of the boundaries are free of loading implying zero natural boundary conditions.

The full-field finite element models are described by three classical material constants (two elastic moduli and one thermal expansion coefficient) and discretized by the second order tetrahedral elements C3D10MT with full integration, see the details in Table 13. The microarchitected plates are then modelled by the strain gradient Reissner–Mindlin plates of the equivalent homogenized continuum and discretized by 64 (8×8) finite elements with NURBS basis functions of the fifth order with C^4-continuity and described by constitutive matrices $\mathbf{C}^1$ and $\mathbf{C}^2$ (see Section 3.1) and $\mathbf{A}^R$ (see Section 3.4). The model contains nine elastic constants in total (five classical and four higher-order ones) as well as one coefficient of thermal expansion. Stress and strain vectors as well as constitutive matrices undergo the corresponding transformations as detailed in [82]. The specific heat capacity and thermal conductivity are not affecting the temperature distributions in this case and, hence, are not specified.

Table 13: FE plate model characteristics. NFE stands for the number of finite elements and NDF for the number of (translational) degrees of freedom. Numbers are rounded except for the IGA model.

	Square		Circular		Annular		IGA
	$N=1$	$N=2$	$N=1$	$N=2$	$N=1$	$N=2$	model
NFE	$0.2 \cdot 10^6$	$0.4 \cdot 10^6$	$0.2 \cdot 10^6$	$0.4 \cdot 10^6$	$0.2 \cdot 10^6$	$0.3 \cdot 10^6$	64
NDF	$1.1 \cdot 10^6$	$2.1 \cdot 10^6$	$1.2 \cdot 10^6$	$2.3 \cdot 10^6$	$0.9 \cdot 10^6$	$1.8 \cdot 10^6$	169

The results of numerical simulations are compared in Fig. 7.1. For visualisation, in Fig. 7.1 (left column) a cut along the plate diagonal AC is shown and part ABC is presented in a transparent view. The region with the applied distributed load is depicted in Fig. 7.1 (bottom right) by grey colour.

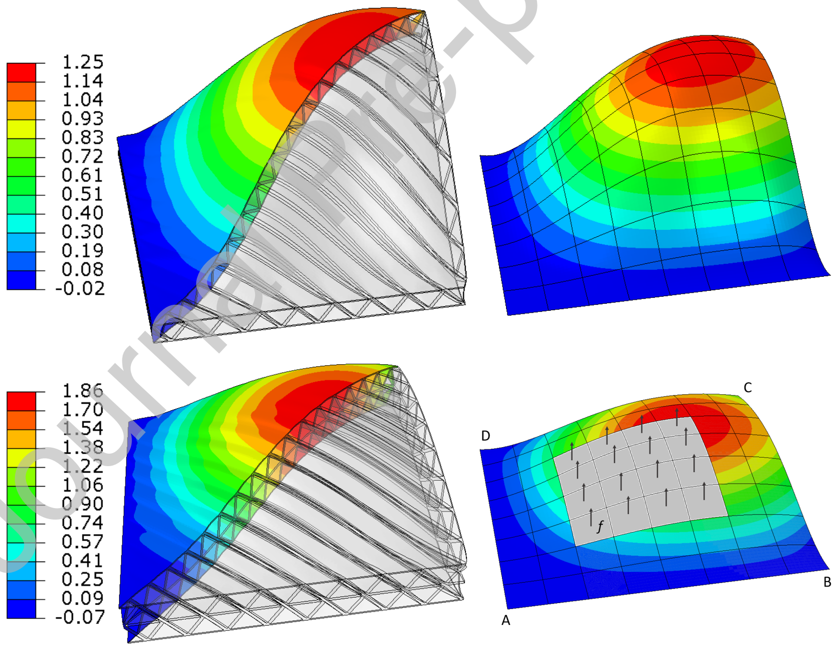

Figure 7.1: Distribution of the normalized displacement field in the mechanically induced bending problem of square plate with a rotated microarchitecture (normalization with respect to the deflection of corner C). Top row: plate thickness $t = 4.33$ mm ($N = 1$). Bottom row: plate thickness $t = 8.66$ mm ($N = 2$). Left column: full-field simulation results. Right column: IGA simulations of the corresponding strain gradient Reissner–Mindlin plate of equivalent continuum. Plate side length is constant ($L = 60$ mm).

Fig. 7.2 shows the distribution of the transversal displacements along the plate diagonal AC where the blue dots correspond to the full-field simulation results, the red curve represents the reduced strain gradient thermoelastic Reissner–Mindlin plate model results and the black line stands for the results of the corresponding classical plate model. As can be seen, the microarchitected plate bending response is captured both qualitatively and, most importantly, quantitatively by the strain gradient plate model (with the equivalent continuum) with a high precision. The classical plate model, or actually the classical thermoelasticity theory, fails to properly describe the bending response by significantly overestimating the displacement field.

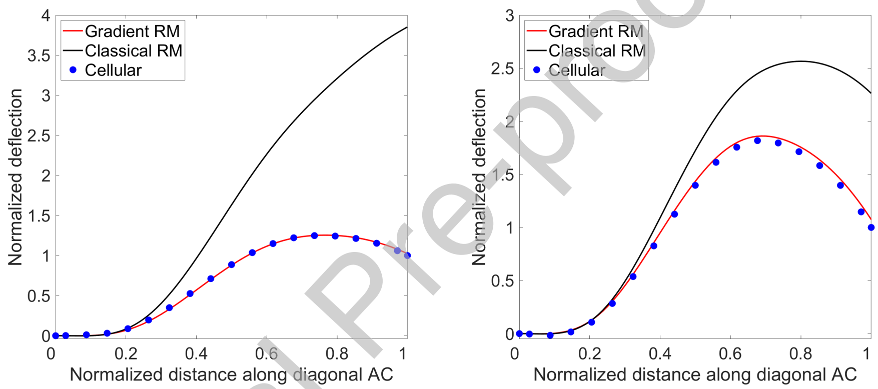

Figure 7.2: Normalized deflection (with respect to the deflection of corner C) versus normalized distance (with respect to the diagonal length) along plate diagonal AC in the thermomechanical bending problem of a clamped square plate. Left: plate thickness $t = 4.33$ mm ($N = 1$). Right: plate thickness $t = 8.66$ mm ($N = 2$). Full-field simulation results (blue dots) are compared with the reduced strain gradient (red curve) and classical (black line) Reissner–Mindlin plate models.

7.2. Circular plate

As the next example, we consider a circular plate (Fig. 7.3) made of isotropic steel with material properties listed in Table 1. The global Cartesian coordinate system is placed such that the plate midsurface has $z = 0$ and coordinate axes x and y lie in the midsurface plane. The microarchitecture is oriented such that the local coordinate axes x_1 and x_2 coincide, respectively, with coordinate axes x and y (see Fig. 5.1b). Two types of microarchitected plates with $N = 1$ and 2, or $t = 4.33$ mm and 8.66 mm, are constructed such that the plate radius R is kept constant ($R = 50$ mm).

For the mechanically induced bending, the plate circuit is clamped, whereas uniformly distributed load is applied in the transversal direction. The full-field finite element models are discretized by the second order tetrahedral elements C3D10 with full integration. The corresponding strain gradient plate is discretized by only 64 (8×8) finite elements with NURBS basis functions of the fifth order with C^4-continuity. The results of numerical simulations are shown and compared in Fig. 7.3.

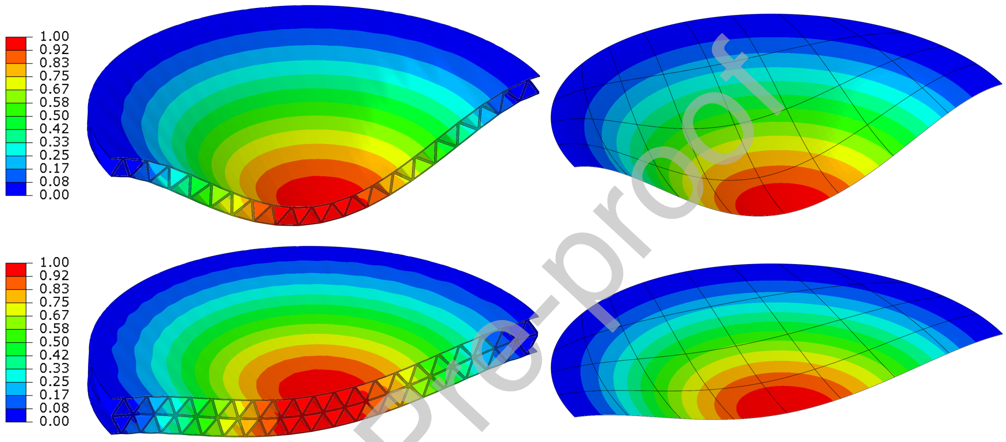

Figure 7.3: Distribution of the normalized (with respect to the deflection of the middle point) displacement field in the mechanically induced bending problem of a clamped circular plate. Top row: plate thickness $t = 4.33$ mm ($N = 1$). Bottom row: plate thickness $t = 8.66$ mm ($N = 2$). Left column: full-field simulation results. Right column: IGA simulations of the corresponding strain gradient Reissner–Mindlin plate of equivalent continuum. Plate radius is kept constant ($R = 50$ mm). For visualisation purposes, view cut along the plate diameter is presented.

Fig. 7.4 shows the distribution of the transversal displacements along the plate diameter perpendicular to the microarchitecture direction x_2 (cf. Fig. 5.1). The blue dots correspond to the full-field simulation results, the red curve represents the reduced strain gradient Reissner–Mindlin plate model results and the black line stands for the results of the corresponding classical plate model. As can be seen, the classical elasticity theory fails to capture the bending response as it significantly overestimates the displacement field.

For the thermally induced bending, the plate circuit is simply supported, whereas constant temperatures $+T_0$ and $-T_0$ are prescribed, respectively, at the upper ($z = -t/2$) and lower ($z = t/2$) surfaces. The results of numerical simulations are presented and compared in Fig. 7.5.

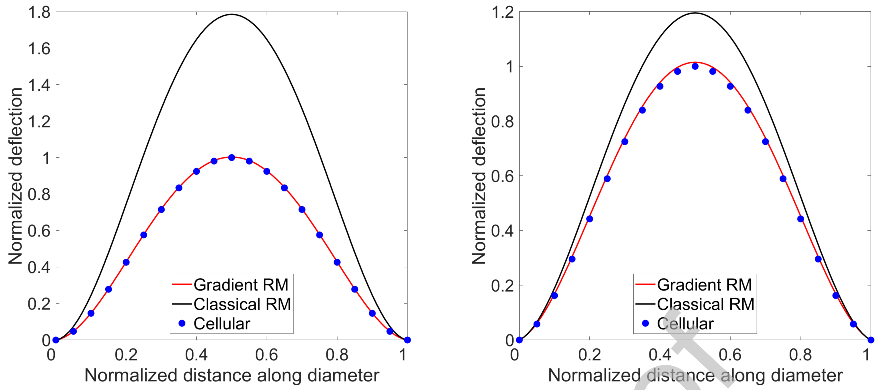

Figure 7.4: Normalized deflection (with respect to the deflection of the middle point) versus normalized distance along diameter of the plate in the mechanically induced bending problem of a clamped circular plate. Left: plate thickness $t = 4.33$ mm ($N = 1$). Right: plate thickness $t = 8.66$ mm ($N = 2$). Full-field simulation results (blue dots) are compared with the reduced strain gradient (red curve) and classical (black line) Reissner–Mindlin plate models.

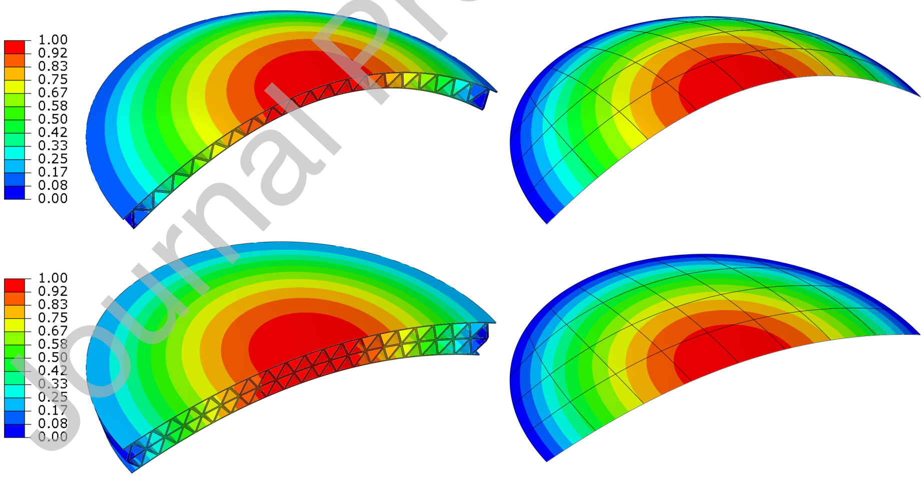

Figure 7.5: Distribution of the normalized (with respect to the deflection of the middle point) displacement field in the thermally induced bending problem of a simply supported circular plate. Top row: plate thickness $t = 4.33$ mm ($N = 1$). Bottom row: plate thickness $t = 8.66$ mm ($N = 2$). Left column: full-field simulation results. Right column: IGA simulations of the corresponding strain gradient Reissner–Mindlin plate of equivalent continuum. Plate radius is kept constant ($R = 50$ mm). For visualisation purposes, view cut along the plate diameter is presented.

Fig. 7.6 presents the distribution of the transversal displacements along the plate diameter perpendicular to the microarchitecture direction x_2 (cf. Fig. 5.1). The red curve relates to the plate model of Section 3.4 developed in the framework of the complete, or consistent, thermoelastic material model [29]. The black line now corresponds to the reduced strain gradient Reissner–Mindlin plate model within the incomplete, or inconsistent, thermoelastic material model. This means that the temperature gradient is not introduced in the Helmholtz free energy and, hence, is not included in the constitutive law for double stresses. As a result, the corresponding plate model significantly underestimates the bending response of the microarchitectural plate (as has been discovered by the authors in [29] for microarchitectural beams).

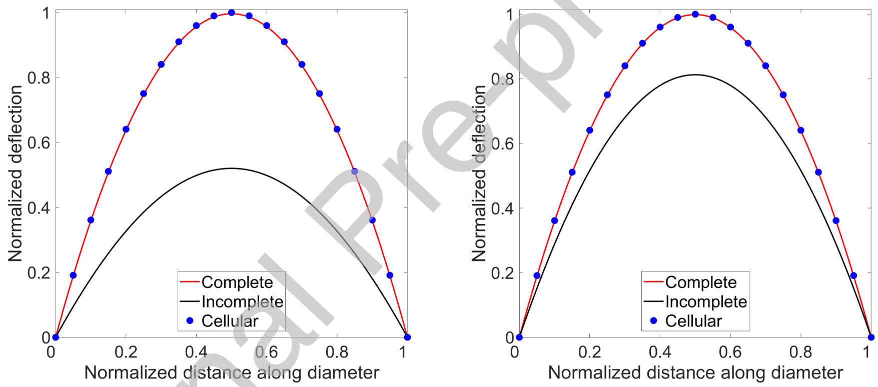

Figure 7.6: Normalized deflection (with respect to the middle point deflection) versus normalized distance along diameter of the plate in the thermally induced bending problem of a simply supported circular plate. Left: plate thickness $t = 4.33$ mm ($N = 1$). Right: plate thickness $t = 8.66$ mm ($N = 2$). Full-field simulation results (blue dots) are compared with the reduced strain gradient Reissner–Mindlin plate model in the framework of complete (red curve) and incomplete (black line) thermoelastic gradient problem formulation.

7.3. Annular plate

As the last example, we consider a quadrant of an annular plate (Fig. 7.7) made of isotropic steel with material properties listed in Table 1. The global Cartesian coordinate system is placed such that the plate midsurface has $z = 0$, coordinate axes x and y lie along the plate sides AB and CD, respectively (see Fig. 7.7). The microarchitecture is oriented such that the local coordinate axes x_1 and x_2 (see Fig. 5.1b) are parallel, respectively, to coordinate axes x and y. Two types of microarchitected plates with $N = 1$ and 2, or $t = 4.33$ mm and 8.66 mm, are constructed such that the plate radii are kept constant (inner radius $R_i = 50$ mm and outer radius $R_o = 100$ mm).

For the mechanically induced bending, sides AB and CD are clamped, whereas a uniformly distributed load is applied in the transversal direction. The full-field finite element models are discretized by the second order tetrahedral elements C3D10 with full integration. The corresponding strain gradient plate is discretized by 64 finite elements with NURBS basis functions of the fifth order with C^4-continuity. The results of numerical simulations are shown in Fig. 7.7 in which the normalization is performed with respect to the maximum deflection located at point K. A plot of the transversal displacements along the annular plate side BC is shown in Fig. 7.8 for the plates of the first type with $N = 1$ (left) and second type with $N = 2$ (right).

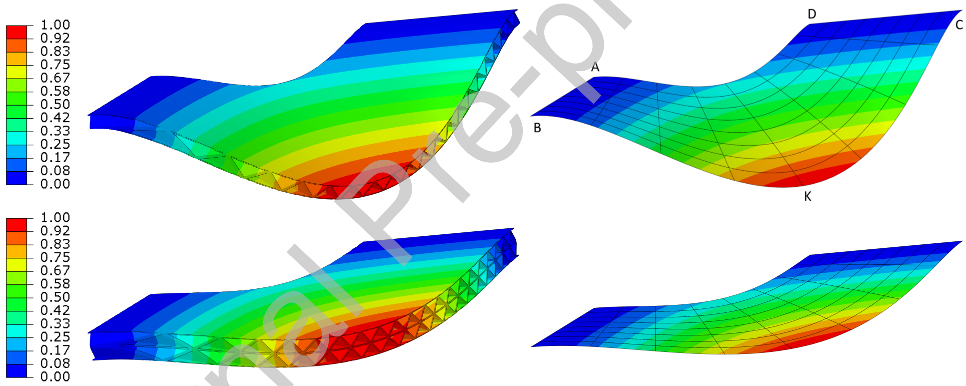

Figure 7.7: Distribution of the normalized (with respect to the maximum deflection located at point K) displacement field in the mechanically induced bending problem of a clamped annular plate. Top row: plate thickness $t = 4.33$ mm ($N = 1$). Bottom row: plate thickness $t = 8.66$ mm ($N = 2$). Left column: full-field simulation results. Right column: IGA simulations of the corresponding strain gradient Reissner–Mindlin plate of equivalent continuum. Plate radii are kept constant ($R_i = 50$ mm and $R_o = 100$ mm).

For thermally induced bending, side CD is clamped, whereas constant temperatures $+T_0$ and $-T_0$ are prescribed, respectively, at the upper ($z = -t/2$) and lower ($z = t/2$) surfaces. The results of numerical simulations are presented and compared in Fig. 7.9 in which the normalization is performed with respect to the deflections at the plate corner B. A plot of the transversal displacements along the annular plate side CB is depicted in Fig. 7.10 for the plates of the first type with $N = 1$ (left) and second type with $N = 2$ (right).

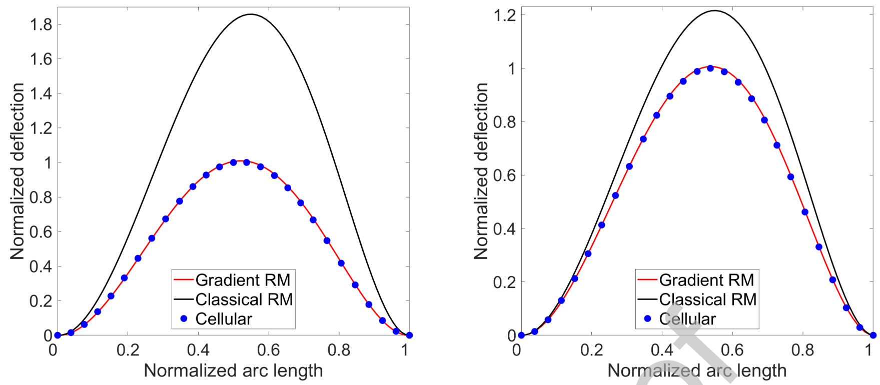

Figure 7.8: Normalized deflection of plate edge BC versus normalized arc length (starting from corner B) of the corresponding circular segment in the mechanically induced bending problem of a clamped annular plate. Left: plate thickness $t = 4.33$ mm ($N = 1$). Right: plate thickness $t = 8.66$ mm ($N = 2$). Full-field simulation results (blue dots) are compared with the reduced strain gradient (red curve) and classical (black line) Reissner–Mindlin plate models.

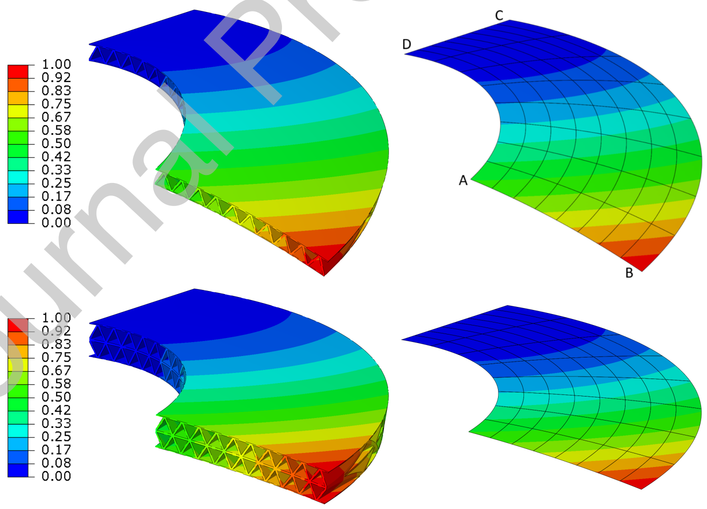

Figure 7.9: Distribution of the normalized (with respect to the maximum deflections at the plate corner B) displacement field in the thermally induced bending problem of a clamped annular plate. Top row: plate thickness $t = 4.33$ mm ($N = 1$). Bottom row: plate thickness $t = 8.66$ mm ($N = 2$). Left column: full-field simulation results. Right column: IGA simulations of the corresponding strain gradient Reissner–Mindlin plate of equivalent continuum. Plate radii are kept constant ($R_i = 50$ mm and $R_o = 100$ mm).

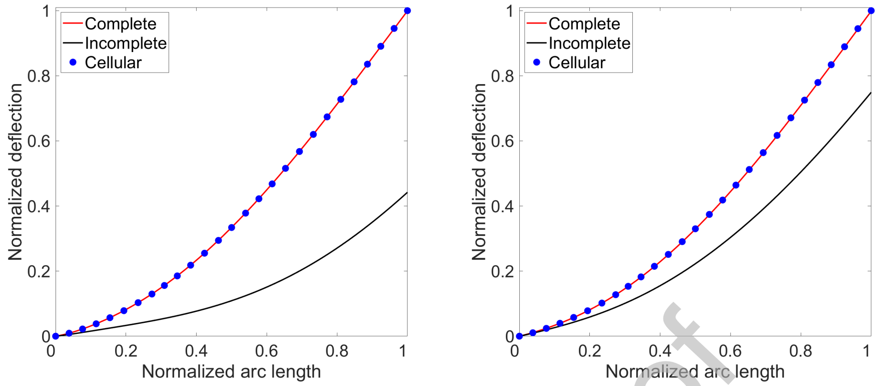

Figure 7.10: Normalized deflection of edge BC versus normalized arc length (starting from corner C) of the corresponding circular segment in the thermally induced bending problem of a clamped annular plate. Left: plate thickness $t = 4.33$ mm ($N = 1$). Right: plate thickness $t = 8.66$ mm ($N = 2$). Full-field simulation results (blue dots) are compared with the reduced strain gradient Reissner–Mindlin plate model in the framework of complete (red curve) and incomplete (black line) thermoelastic strain gradient problem formulation.

8. Conclusions and discussion

This work is a part of the development and investigation of the applicability of generalized continuum theories in the context of thermomechanics of solids, structures, materials and meta-materials. In this respect, the content of the work can be summarized as follows – listing at the same time the main novelties of this contribution:

1. An orthotropic version of the Mindlin type three-dimensional strain gradient thermoelasticity theory has been formulated.
2. A pair of two-dimensional plate models – the Kirchhoff and Reissner–Mindlin types – relying on the orthotropic strain gradient thermoelasticity has been derived for the modeling of thin and thick microarchitectural plate-like structures. In addition to dimension reduction, the plate models have been constitutively reduced in order to minimize the number of the generalized constitutive parameters. Having conforming Galerkin discretizations in mind, the plate models have been formulated as variational problems.
3. A computational homogenization method has been proposed for determining the constitutive parameters of the related higher-order constitutive tensors. Classical constitutive parameters have been obtained via a computational homogenization method as well.

4. The bending size effects induced by the microarchitecture of cellular plate-like structures are shown to be captured by the generalized plate models in a computationally realiable and efficient way.

Regarding items 1 and 4, we emphasize that this work confirms and illustrates the necessity of including temperature gradients in the Helmholtz free energy within strain gradient elasticity according to [83, 29].

Regarding item 2, we note that as in the case of classical plate models the constitutively reduced strain gradient plate models have been designed to be consistent in the sense that the Kirchhoff model can be seen as the thickness limit of the corresponding Reissner–Mindlin model.

As an outlook, we conclude that locking-free numerical formulations, vibration problems and experimental validation are the next relevant research directions for the present topic. Generalized shell models and nonlinearities of plate- and shell-like microarchitectural structures – having applications in various fields of science and industry – are considered as the most natural extensions for the results of this work. It is evident that nonlinearities (see the framework for the geometrical ones in [84]), whether they are geometrical or material, have both local and global effects on the structure and its microarchitecture during nonlinear deformations such as large displacements or rotations, buckling, yielding and damage, in particular. Therefore, it is most likely impossible to govern the consequences of all possible local deformation mechanisms by one general constitutive framework. Regarding item 3 above, this implies challenges for the parameter identification within the nonlinear regime. Brittle damage is probably the most straightforward topic of nonlinearities as long as it can be handled via a scalar deterioration parameter (cf. [85]).

Acknowledgements

The authors have been supported by Academy of Finland through the project *Adaptive isogeometric methods for thin-walled structures* (decision numbers 270007, 304122). The second author gratefully acknowledges the support of the August-Wilhelm Scheer Visiting Professors Program established by TUM International Center and funded by the German Excellence Initiative. Access and licenses for the commercial FE software Abaqus have been provided by CSC – IT Center for Science (www.csc.fi).

Appendices

A. On plane assumptions for Cauchy stresses

For brevity, we set $\theta = 0$, which does not affect the following derivations. By adopting the plane stress assumption expressed as $\sigma_{zz} = 0$, one can eliminate ε_{zz} rewritten as

$$\varepsilon_{zz} = -\frac{\hat{C}_{13}}{\hat{C}_{33}}\varepsilon_{xx} - \frac{\hat{C}_{23}}{\hat{C}_{33}}\varepsilon_{yy} \tag{A.1}$$

from the constitutive law (2.7) resulting in relation (3.3) corresponding to the Reissner–Mindlin plate model. For this case, the classical elasticity constants are defined as follows:

$$\begin{aligned} C_{11} &= \frac{\hat{C}_{11}\hat{C}_{33} - \hat{C}_{13}^2}{\hat{C}_{33}}, \quad C_{22} = \frac{\hat{C}_{22}\hat{C}_{33} - \hat{C}_{23}^2}{\hat{C}_{33}}, \\ C_{12} &= \frac{\hat{C}_{12}\hat{C}_{33} - \hat{C}_{13}\hat{C}_{23}}{\hat{C}_{33}}, \quad C_{66} = \hat{C}_{66}. \end{aligned} \tag{A.2}$$

Concerning the $\mathbf{C}^2$-stiffness matrix in expression (3.3), its components are multiplied by the classical shear correction factor κ ($\kappa = 0.85$ [86]):

$$C_{44} = \kappa\hat{C}_{44}, \quad C_{55} = \kappa\hat{C}_{55}. \tag{A.3}$$

B. On plane assumptions for double stresses

As in Appendix A, we set $\theta = 0$. By adopting the plane assumption proposed in Section 3.1 with respect to double stresses, i.e., $\mu_{zzx} = \mu_{zzy} = \mu_{zzz} = \mu_{xzz} = \mu_{yzz} = 0$, one can eliminate $\varepsilon_{zz,x}$, $\varepsilon_{zz,y}$, $\varepsilon_{zz,z}$, $\varepsilon_{xz,z}$ and $\varepsilon_{yz,z}$

from the constitutive law (2.10) and write

$$
\begin{aligned}
\varepsilon_{zz,x} &= \frac{\hat{a}^1_{15}\hat{a}^1_{45} - \hat{a}^1_{14}\hat{a}^1_{55}}{\hat{a}^1_{44}\hat{a}^1_{55} - (\hat{a}^1_{45})^2}\varepsilon_{xx,x} + \frac{\hat{a}^1_{25}\hat{a}^1_{45} - \hat{a}^1_{24}\hat{a}^1_{55}}{\hat{a}^1_{44}\hat{a}^1_{55} - (\hat{a}^1_{45})^2}\varepsilon_{yy,x} + \frac{\hat{a}^1_{35}\hat{a}^1_{45} - \hat{a}^1_{34}\hat{a}^1_{55}}{\hat{a}^1_{44}\hat{a}^1_{55} - (\hat{a}^1_{45})^2}\varepsilon_{xy,y} \\
\varepsilon_{xz,z} &= \frac{\hat{a}^1_{14}\hat{a}^1_{45} - \hat{a}^1_{15}\hat{a}^1_{44}}{\hat{a}^1_{44}\hat{a}^1_{55} - (\hat{a}^1_{45})^2}\varepsilon_{xx,x} + \frac{\hat{a}^1_{24}\hat{a}^1_{45} - \hat{a}^1_{25}\hat{a}^1_{44}}{\hat{a}^1_{44}\hat{a}^1_{55} - (\hat{a}^1_{45})^2}\varepsilon_{yy,x} + \frac{\hat{a}^1_{34}\hat{a}^1_{45} - \hat{a}^1_{35}\hat{a}^1_{44}}{\hat{a}^1_{44}\hat{a}^1_{55} - (\hat{a}^1_{45})^2}\varepsilon_{xy,y} \\
\varepsilon_{zz,y} &= \frac{\hat{a}^2_{15}\hat{a}^2_{45} - \hat{a}^2_{14}\hat{a}^2_{55}}{\hat{a}^2_{44}\hat{a}^2_{55} - (\hat{a}^2_{45})^2}\varepsilon_{yy,y} + \frac{\hat{a}^2_{25}\hat{a}^2_{45} - \hat{a}^2_{24}\hat{a}^2_{55}}{\hat{a}^2_{44}\hat{a}^2_{55} - (\hat{a}^2_{45})^2}\varepsilon_{xx,y} + \frac{\hat{a}^2_{35}\hat{a}^2_{45} - \hat{a}^2_{34}\hat{a}^2_{55}}{\hat{a}^2_{44}\hat{a}^2_{55} - (\hat{a}^2_{45})^2}\varepsilon_{xy,x} \\
\varepsilon_{yz,z} &= \frac{\hat{a}^2_{14}\hat{a}^2_{45} - \hat{a}^2_{15}\hat{a}^2_{44}}{\hat{a}^2_{44}\hat{a}^2_{55} - (\hat{a}^2_{45})^2}\varepsilon_{yy,y} + \frac{\hat{a}^2_{24}\hat{a}^2_{45} - \hat{a}^2_{25}\hat{a}^2_{44}}{\hat{a}^2_{44}\hat{a}^2_{55} - (\hat{a}^2_{45})^2}\varepsilon_{xx,y} + \frac{\hat{a}^2_{34}\hat{a}^2_{45} - \hat{a}^2_{35}\hat{a}^2_{44}}{\hat{a}^2_{44}\hat{a}^2_{55} - (\hat{a}^2_{45})^2}\varepsilon_{xy,x} \\
\varepsilon_{zz,z} &= -\frac{\hat{a}^3_{12}}{\hat{a}^3_{11}}\varepsilon_{xx,z} - \frac{\hat{a}^3_{13}}{\hat{a}^3_{11}}\varepsilon_{xz,x} - \frac{\hat{a}^3_{14}}{\hat{a}^3_{11}}\varepsilon_{yy,z} - \frac{\hat{a}^3_{15}}{\hat{a}^3_{11}}\varepsilon_{yz,y}
\end{aligned} \tag{B.1}
$$

resulting in relation (3.6) corresponding to the Reissner–Mindlin plate model. The higher-order plane elasticity moduli corresponding to matrices $\mathbf{A}^1$ and $\mathbf{A}^2$ are defined in the form $(i = 1, 2)$

$$
\begin{aligned}
a^i_{11} &= \hat{a}^i_{11} - \frac{\hat{a}^i_{14}\,(\hat{a}^i_{14}\,\hat{a}^i_{55} - \hat{a}^i_{15}\,\hat{a}^i_{45})}{\hat{a}^i_{44}\,\hat{a}^i_{55} - (\hat{a}^i_{45})^2} + \frac{\hat{a}^i_{15}\,(\hat{a}^i_{14}\,\hat{a}^i_{45} - \hat{a}^i_{15}\,\hat{a}^i_{44})}{\hat{a}^i_{44}\,\hat{a}^i_{55} - (\hat{a}^i_{45})^2}, \\
a^i_{12} &= \hat{a}^i_{12} - \frac{\hat{a}^i_{14}\,(\hat{a}^i_{24}\,\hat{a}^i_{55} - \hat{a}^i_{25}\,\hat{a}^i_{45})}{\hat{a}^i_{44}\,\hat{a}^i_{55} - (\hat{a}^i_{45})^2} + \frac{\hat{a}^i_{15}\,(\hat{a}^i_{24}\,\hat{a}^i_{45} - \hat{a}^i_{25}\,\hat{a}^i_{44})}{\hat{a}^i_{44}\,\hat{a}^i_{55} - (\hat{a}^i_{45})^2}, \\
a^i_{13} &= \hat{a}^i_{13} - \frac{\hat{a}^i_{14}\,(\hat{a}^i_{34}\,\hat{a}^i_{55} - \hat{a}^i_{35}\,\hat{a}^i_{45})}{\hat{a}^i_{44}\,\hat{a}^i_{55} - (\hat{a}^i_{45})^2} + \frac{\hat{a}^i_{15}\,(\hat{a}^i_{34}\,\hat{a}^i_{45} - \hat{a}^i_{35}\,\hat{a}^i_{44})}{\hat{a}^i_{44}\,\hat{a}^i_{55} - (\hat{a}^i_{45})^2}, \\
a^i_{22} &= \hat{a}^i_{22} - \frac{\hat{a}^i_{24}\,(\hat{a}^i_{24}\,\hat{a}^i_{55} - \hat{a}^i_{25}\,\hat{a}^i_{45})}{\hat{a}^i_{44}\,\hat{a}^i_{55} - (\hat{a}^i_{45})^2} + \frac{\hat{a}^i_{25}\,(\hat{a}^i_{24}\,\hat{a}^i_{45} - \hat{a}^i_{25}\,\hat{a}^i_{44})}{\hat{a}^i_{44}\,\hat{a}^i_{55} - (\hat{a}^i_{45})^2}, \\
a^i_{23} &= \hat{a}^i_{23} - \frac{\hat{a}^i_{24}\,(\hat{a}^i_{34}\,\hat{a}^i_{55} - \hat{a}^i_{35}\,\hat{a}^i_{45})}{\hat{a}^i_{44}\,\hat{a}^i_{55} - (\hat{a}^i_{45})^2} + \frac{\hat{a}^i_{25}\,(\hat{a}^i_{34}\,\hat{a}^i_{45} - \hat{a}^i_{35}\,\hat{a}^i_{44})}{\hat{a}^i_{44}\,\hat{a}^i_{55} - (\hat{a}^i_{45})^2}, \\
a^i_{33} &= \hat{a}^i_{33} - \frac{\hat{a}^i_{34}\,(\hat{a}^i_{34}\,\hat{a}^i_{55} - \hat{a}^i_{35}\,\hat{a}^i_{45})}{\hat{a}^i_{44}\,\hat{a}^i_{55} - (\hat{a}^i_{45})^2} + \frac{\hat{a}^i_{35}\,(\hat{a}^i_{34}\,\hat{a}^i_{45} - \hat{a}^i_{35}\,\hat{a}^i_{44})}{\hat{a}^i_{44}\,\hat{a}^i_{55} - (\hat{a}^i_{45})^2}.
\end{aligned} \tag{B.2}
$$

The $\mathbf{A}^4$-stiffness matrix remains unchanged, i.e., $\mathbf{A}^4 = \hat{\mathbf{A}}^4$. It should be noted that the shear correction factors corresponding to double stresses are not addressed. Details are omitted here since the higher-order moduli affected by the shear correction factor do not appear in the reduced plate models.

Concerning the $\mathbf{A}^3$-stiffness matrix, the components are derived as

$$
\begin{aligned}
&a^3_{11} = \hat{a}^3_{22} - \frac{(\hat{a}^3_{12})^2}{\hat{a}^3_{11}}, \quad a^3_{12} = \hat{a}^3_{23} - \frac{\hat{a}^3_{12}\,\hat{a}^3_{13}}{\hat{a}^3_{11}}, \quad a^3_{13} = \hat{a}^3_{24} - \frac{\hat{a}^3_{12}\,\hat{a}^3_{14}}{\hat{a}^3_{11}},\\
&a^3_{14} = \hat{a}^3_{25} - \frac{\hat{a}^3_{12}\,\hat{a}^3_{15}}{\hat{a}^3_{11}}, \quad a^3_{22} = \hat{a}^3_{33} - \frac{(\hat{a}^3_{13})^2}{\hat{a}^3_{11}}, \quad a^3_{23} = \hat{a}^3_{34} - \frac{\hat{a}^3_{13}\,\hat{a}^3_{14}}{\hat{a}^3_{11}},\\
&a^3_{24} = \hat{a}^3_{35} - \frac{\hat{a}^3_{13}\,\hat{a}^3_{15}}{\hat{a}^3_{11}}, \quad a^3_{33} = \hat{a}^3_{44} - \frac{(\hat{a}^3_{14})^2}{\hat{a}^3_{11}}, \quad a^3_{34} = \hat{a}^3_{45} - \frac{\hat{a}^3_{14}\,\hat{a}^3_{15}}{\hat{a}^3_{11}},\\
&a^3_{44} = \hat{a}^3_{55} - \frac{(\hat{a}^3_{15})^2}{\hat{a}^3_{11}}.
\end{aligned} \tag{B.3}
$$

C. Analytical solutions for Reissner–Mindlin plates

For a plate of infinite width in the y-direction (see Fig. 6.1a), bended along the x-direction, the kinematical variables can be assumed as follows:

$$
w = w(x), \quad \beta_x = \beta_x(x), \quad \beta_y = 0. \tag{C.1}
$$

For the considered problem, the variational formulation of Section 3.4 reduces to a one-dimensional form with the load functional and bilinear form written as

$$
\begin{aligned}
a(w, \beta_x; \hat{w}, \hat{\beta}_x) = b \int_0^L &((D_{11} + R_{11})\beta_{x,x}\hat{\beta}_{x,x}\\
&+ D_{55}(w_{,x} - \beta_x)(\hat{w}_{,x} - \hat{\beta}_x))\mathrm{d}x,
\end{aligned} \tag{C.2}
$$

$$
l(\hat{w}, \hat{\beta}_x) = bQ_1\hat{w}|_0^L + bM_x\hat{\beta}_x|_0^L, \tag{C.3}
$$

where b stands for the plate width in the y-direction, L denotes the plate length in the x-direction, the classical bending rigidities $D_{11} = C_{11}t^3/12$ and $D_{55} = tC_{55}$ are defined by (3.18) and the higher-order bending rigidity $R_{11} = ta^3_{11}$ is calculated via (3.31) considering constant elastic moduli.

The corresponding strong form is given by the differential equations

$$
\begin{cases}
0 &= (D_{11} + R_{11})\beta_{x,xx} + D_{55}(w_{,x} - \beta_x)\\
0 &= D_{55}(w_{,xx} - \beta_{x,x})
\end{cases}, \quad \forall x \in (0, L) \tag{C.4}
$$

and boundary conditions at $x = 0, L$ as

$$w = \bar{w} \quad \text{or} \quad Q_1 = D_{55}(w_{,x} - \beta_x), \tag{C.5}$$
$$\beta_x = \bar{\beta}_x \quad \text{or} \quad M_x = (D_{11} + R_{11})\beta_{x,x}, \tag{C.6}$$

where $\bar{w}$ and $\bar{\beta}_x$ denote the given data on the boundaries. The analytical solution of system (C.4) takes a general form

$$\begin{cases} w(x) & = A_4x^3 + A_3x^2 + A_2x + A_1 \\ \beta_x(x) & = 3A_4x^2 + 6A_4(D_{11} + R_{11})/D_{55} + 2A_3x + A_2 \end{cases}. \tag{C.7}$$

For a simply supported plate loaded by bending moments at $x = 0, L$, boundary conditions are written as $w(0) = w(L) = 0$ and $M_x(0) = M_x(L) = -M_0$, leading to the following expressions for integration constants A_i:

$$A_3 = -\frac{M_0}{2(D_{11} + R_{11})}, \quad A_2 = -A_3L, \quad A_1 = 0, \quad A_4 = 0. \tag{C.8}$$

Bending rigidity is calculated by

$$D_{gr} = -\frac{M_0}{t^2\varphi_L}, \quad \text{where} \quad \varphi_L = \beta_x(L). \tag{C.9}$$

By substituting the analytical solution (C.7) with (C.8) in expression (C.9), bending rigidity can be written in terms of plate model rigidities as

$$D_{gr} = \frac{2}{t^2L}(D_{11} + R_{11}), \tag{C.10}$$

or equivalently in terms of material moduli as

$$D_{gr} = \frac{t}{6L}(C_{11} + \frac{12}{t^2}a^3_{11}). \tag{C.11}$$

It should be noted that for plates bended along the y-direction the corresponding analytical expression for bending rigidity includes elastic moduli C_{22} and a^3_{33} instead of C_{11} and a^3_{11}, respectively:

$$D_{gr} = \frac{t}{6L}(C_{22} + \frac{12}{t^2}a^3_{33}). \tag{C.12}$$

For a cantilever plate loaded by bending forces at the free edge, boundary conditions are written as $w(0) = 0$, $\beta_x(0) = 0$, $Q_1(L) = F$ and $M_x(L) = 0$, leading to the following expressions for integration constants A_i:

$$A_4 = -\frac{F}{6(D_{11} + R_{11})}, \quad A_3 = -3A_4 L, \quad A_2 = \frac{F}{D_{55}}, \quad A_1 = 0. \tag{C.13}$$

Bending rigidity is calculated by expression

$$D_{gr} = \frac{F}{w_L}, \quad \text{where} \quad w_L = w(L). \tag{C.14}$$

By substituting the analytical solution (C.7) with (C.13) in expression (C.14), bending rigidity can be written in terms of plate model rigidities as

$$D_{gr} = \frac{3(D_{11} + R_{11})D_{55}}{L(L^2 D_{55} + 3D_{11} + 3R_{11})}, \tag{C.15}$$

or equivalently in terms of material moduli as

$$D_{gr} = \frac{t}{L} \frac{(C_{11} + \frac{12}{t^2} a_{11}^3) C_{55}}{4C_{55}\frac{L^2}{t^2} + C_{11} + \frac{12}{t^2} a_{11}^3}. \tag{C.16}$$

For plates bended along the y-direction, the corresponding analytical expression for bending rigidity includes elastic moduli C_{22}, C_{44} and a_{33}^3 instead of C_{11}, C_{55} and a_{11}^3, respectively:

$$D_{gr} = \frac{t}{L} \frac{(C_{22} + \frac{12}{t^2} a_{33}^3) C_{44}}{4C_{44}\frac{L^2}{t^2} + C_{22} + \frac{12}{t^2} a_{33}^3}. \tag{C.17}$$

D. Analytical solutions for Kirchhoff plates

For a plate of infinite width in the y-direction (see Fig. 6.1a), bended along the x-direction, the kinematical variables can be assumed as simply as

$$w = w(x). \tag{D.1}$$

For the considered problem, the variational formulation of Section 4.4 reduces to a one-dimensional form with the load functional and bilinear form written as

$$a(w, \hat{w}) = b \int_0^L (D_{11} + R_{11}) w_{,xx} \hat{w}_{,xx} \mathrm{d}x, \tag{D.2}$$

$$l(\hat{w}) = bQ_1 \hat{w}|_0^L + bM_x \hat{w}_{,x}|_0^L. \tag{D.3}$$

The corresponding strong form is given by the differential equation

$$0 = (D_{11} + R_{11})w_{,xxxx}, \quad \forall x \in (0, L) \tag{D.4}$$

and boundary conditions at $x = 0, L$ as

$$w = \bar{w} \quad \text{or} \quad Q_1 = -(D_{11} + R_{11})w_{,xxx}, \tag{D.5}$$
$$w_{,x} = \bar{\beta} \quad \text{or} \quad M_x = (D_{11} + R_{11})w_{,xx}, \tag{D.6}$$

where $\bar{w}$ and $\bar{\beta}$ denote the given data on boundaries. The analytical solution of equation (D.4) takes a general form

$$w(x) = A_4x^3 + A_3x^2 + A_2x + A_1. \tag{D.7}$$

For a simply supported plate loaded by bending moments at $x = 0, L$ with boundary conditions $w(0) = w(L) = 0$ and $M_x(0) = M_x(L) = -M_0$, integration constants A_i coincide with the ones of the Reissner–Mindlin plate model in Appendix C giving the same expressions for bending rigidity as in (C.10) and (C.11).

For a cantilever plate loaded by bending forces at the free edge, boundary conditions are written as $w(0) = 0$, $w_{,x}(0) = 0$, $Q_1(L) = F$ and $M_x(L) = 0$, leading to the following expressions for integration constants A_i:

$$A_4 = -\frac{F}{6(D_{11} + R_{11})}, \quad A_3 = -3A_4L, \quad A_2 = 0, \quad A_1 = 0. \tag{D.8}$$

Bending rigidity is calculated by expression

$$D_{gr} = \frac{F}{w_L}, \quad \text{where} \quad w_L = w(L). \tag{D.9}$$

By substituting the analytical solution (D.7) with (D.8) in expression (D.9), bending rigidity can be written in terms of plate model rigidities as

$$D_{gr} = \frac{3}{L^3}(D_{11} + R_{11}), \tag{D.10}$$

or equivalently in terms of material moduli as

$$D_{gr} = \frac{t^3}{4L^3}(C_{11} + \frac{12}{t^2}a^3_{11}). \tag{D.11}$$

For plates bended along the y-direction, the corresponding analytical expression for bending rigidity includes elasticity moduli C_{22} and a^3_{33} instead of C_{11} and a^3_{11}, respectively:

$$D_{gr} = \frac{t^3}{4L^3}(C_{22} + \frac{12}{t^2}a^3_{33}). \tag{D.12}$$

E. a^3_{11}-calibration and bending rigidity plots related to aluminium and concrete as base materials

Bending rigidity plots corresponding to aluminium as the base material are shown in Fig. F.1, whereas Fig. F.2 relates to concrete. The blue dots denote the full-field simulation results with $N = 1, 2, 3, 4$ and 8, or $t =$ 4.33 mm, 8.66 mm, 12.99 mm, 17.32 mm and 34.64 mm, respectively. The red line corresponds to expression (6.1) or (6.2) depending on the boundary condition type. The green line relates to expression (6.3). The higher-order a^3_{11}-modulus is calibrated such that the red line fits to the blue dots. The corresponding values of the modulus are given in Table 7.

F. a^3_{33}-calibration and bending rigidity plots related to aluminium and concrete as base materials

Bending rigidity plots corresponding to aluminium as the base material are shown in Fig. F.3, whereas Fig. F.4 relates to concrete. The blue dots denote the full-field simulation results with $N = 1, 2, 3, 4$ and 8, or $t =$ 4.33 mm, 8.66 mm, 12.99 mm, 17.32 mm and 34.64 mm, respectively. The red line corresponds to expression (6.4) or (6.5) depending on the boundary condition type. The green line relates to expression (6.6). The higher-order a^3_{33}-modulus is calibrated such that the red line fits to the blue dots. The corresponding values of the modulus are given in Table 8.

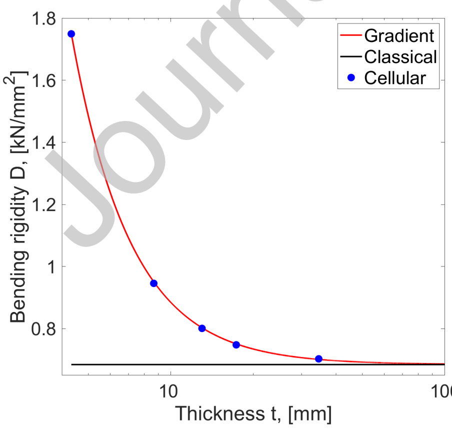

(a) Simply supported case

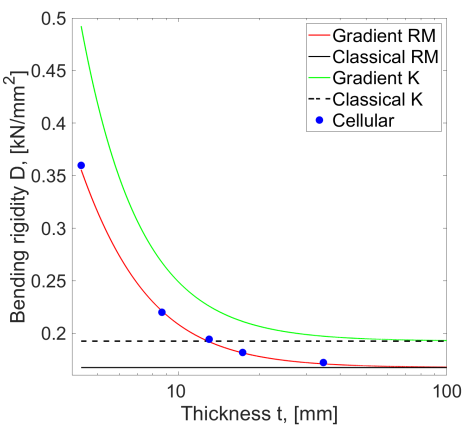

(b) Clamped case

Figure F.1: Bending rigidity versus plate thickness for aluminium.

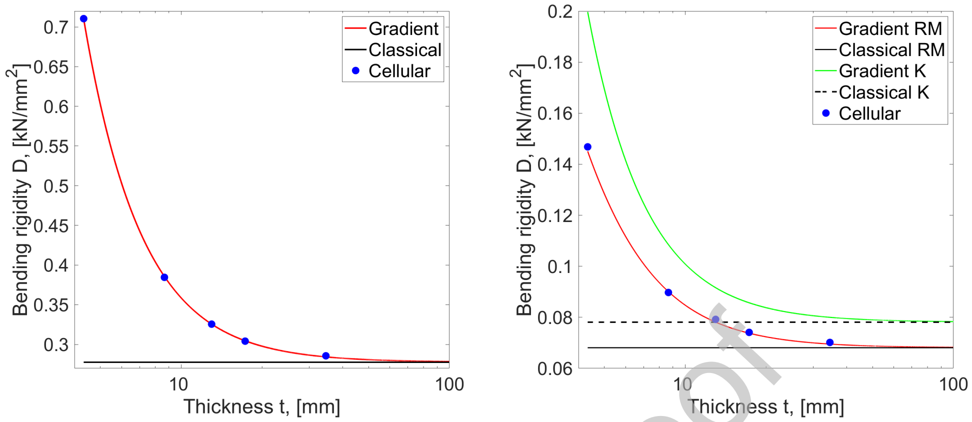

(a) Simply supported case (b) Clamped case

Figure F.2: Bending rigidity versus plate thickness for concrete.

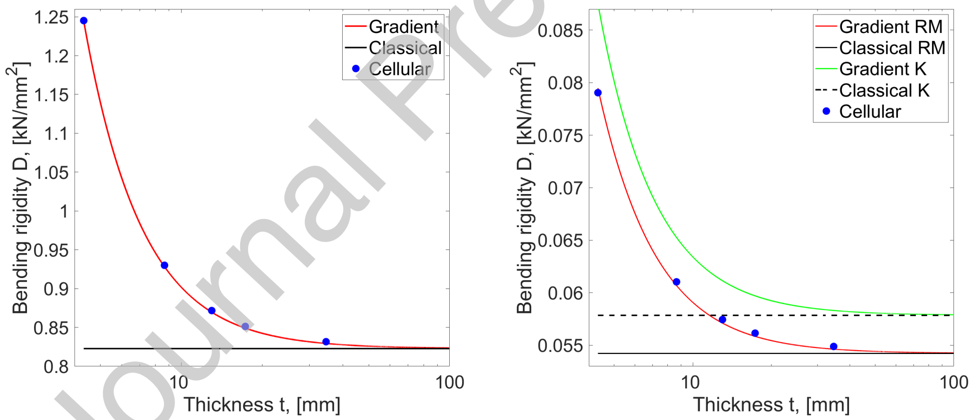

(a) Simply supported case (b) Clamped case

Figure F.3: Bending rigidity versus plate thickness for aluminium.

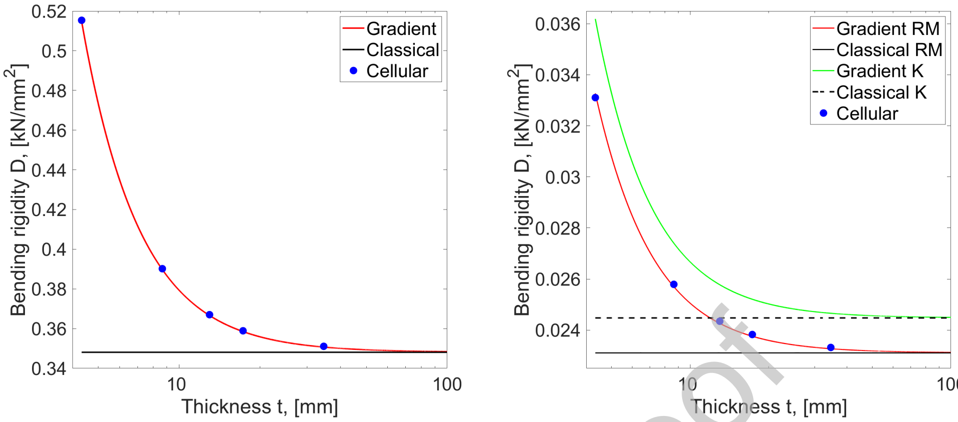

(a) Simply supported case (b) Clamped case

Figure F.4: Bending rigidity versus plate thickness for concrete.

G. a^4_{11}-calibration and bending rigidity plots related to aluminium and concrete as base materials

Bending rigidity plots corresponding to aluminium as the base material are shown in Fig. G.1, whereas Fig. G.2 relates to concrete. The blue dots denote the full-field simulation results with $N = 1, 2, 3$ and 4, or $t = 4.33$ mm, 8.66 mm, 12.99 mm and 17.32 mm, respectively.

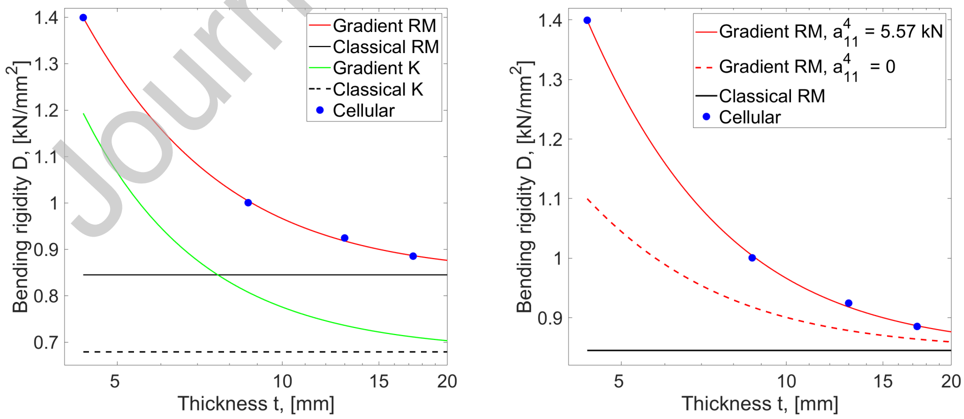

(a) Comparison of plate models. (b) Influence of modulus a^4_{11}.

Figure G.1: Bending rigidity versus plate thickness for aluminium.

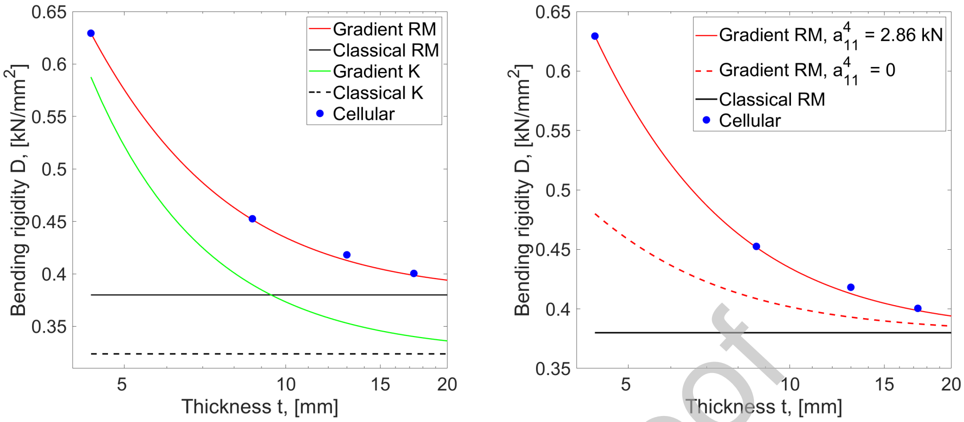

(a) Comparison of plate models. (b) Influence of modulus a^4_{11}.

Figure G.2: Bending rigidity versus plate thickness for concrete.

The red line corresponds to the strain gradient Reissner–Mindlin plate model, while the green curve relates to the strain gradient Kirchhoff plate model. The higher-order a^4_{11}-modulus is calibrated such that the red line fits to the blue dots. The corresponding values of the modulus are given in Table 9.

H. a^3_{13}-calibration and bending rigidity plots related to aluminium and concrete as base materials

Bending rigidity plots corresponding to aluminium as the base material are shown in Fig. H.1, whereas Fig. H.2 relates to concrete. The blue dots denote the full-field simulation results with $N = 1, 2$ and 3, or $t = 4.33$ mm, 8.66 mm and 12.99 mm, respectively. The red line corresponds to the strain gradient Reissner–Mindlin plate model, while the green curve relates to the strain gradient Kirchhoff plate model. The higher-order a^3_{13}-modulus is calibrated such that the red line fits to the blue dots. The corresponding values of the modulus are given in Table 10.

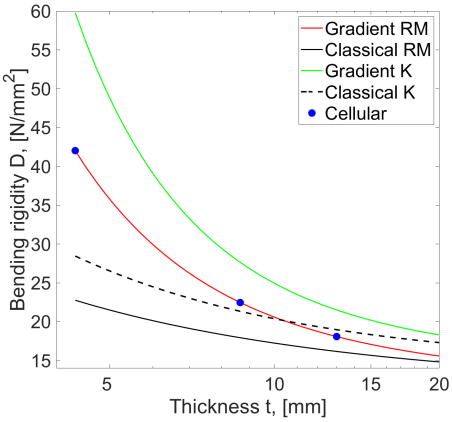

(a) Comparison of plate models.

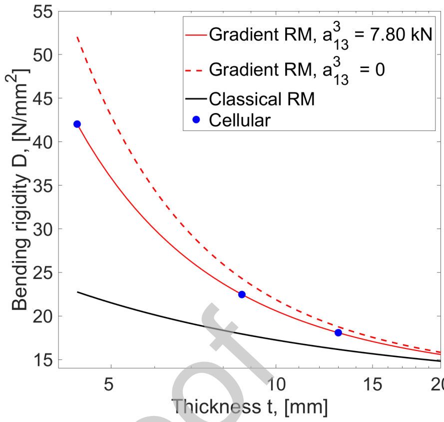

(b) Influence of modulus a^3_{13}.

Figure H.1: Bending rigidity versus plate thickness for aluminium.

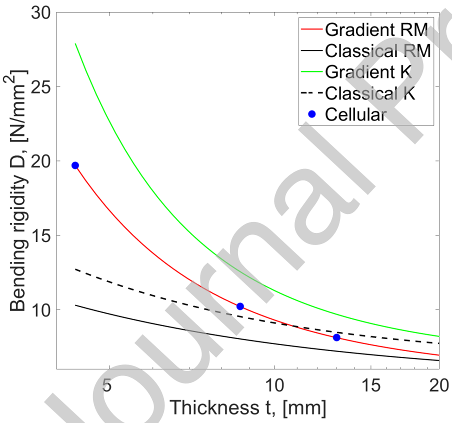

(a) Comparison of plate models.

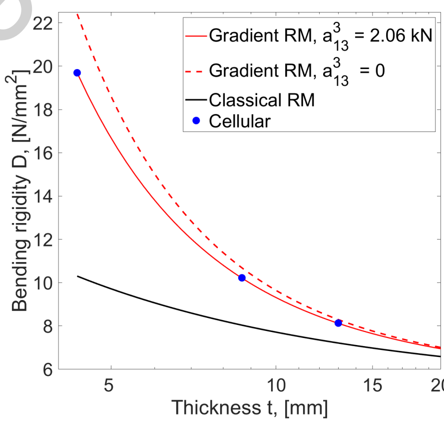

(b) Influence of modulus a^3_{13}.

Figure H.2: Bending rigidity versus plate thickness for concrete.

References

[1] J. Bauer, L. R. Meza, T. A. Schaedler, R. Schwaiger, L. V. X. Zheng, Nanolattices: An emerging class of mechanical metamaterials, Advanced Materials 29 (2017) 1701850.

[2] J. B. Berger, H. N. G. Wadley, R. M. McMeeking, Mechanical metamaterials at the theoretical limit of isotropic elastic stiffness, Nature 543 (2017) 533–537.

[3] M. C. Messner, Optimal lattice-structured materials, Journal of the Mechanics and Physics of Solids 96 (2016) 162–183.

[4] L. R. Meza, G. P. Phlipot, C. M. Portela, A. Maggi, L. C. Montemayor, A. Comella, D. M. Kochmann, J. R. Greer, Reexamining the mechanical property space of three-dimensional lattice architectures, Acta Materialia 140 (2017) 424–432.

[5] G. P. Phlipot, D. M. Kochmann, A quasicontinuum theory for the nonlinear mechanical response of general periodic truss lattices, Journal of the Mechanics and Physics of Solids 124 (2019) 758–780.

[6] M. G. Rashed, M. Ashraf, R. A. W. Mines, P. J. Hazell, Metallic microlattice materials: A current state of the art on manufacturing, mechanical properties and applications, Materials & Design 95 (2016) 518–533.

[7] Q. Zhang, X. Yang, P. Li, G. Huang, S. Feng, C. Shen, B. Han, X. Zhang, F. Jin, F. Xu, T. J. Lu, Bioinspired engineering of honeycomb structure – Using nature to inspire human innovation, Progress in Materials Science 74 (2015) 332–400.

[8] T. A. Schaedler, W. B. Carter, Architected cellular materials, Annual Review of Materials Research 46 (1) (2016) 187–210.

[9] C. M. Spadaccini, Mechanical metamaterials: design, fabrication, and performance, The Bridge 45 (2015) 28–36.

[10] D. D. Vescovo, I. Giorgio, Dynamic problems for metamaterials: Review of existing models and ideas for further research, International Journal of Engineering Science 80 (2014) 153–172.

[11] X. Yu, J. Zhou, H. Liang, Z. Jiang, L. Wu, Mechanical metamaterials associated with stiffness, rigidity and compressibility: A brief review, Progress in Materials Science 94 (2018) 114–173.

[12] G. Dong, Y. Tang, Y. F. Zhao, A survey of modeling of lattice structures fabricated by additive manufacturing, Journal of Mechanical Design 139 (2017) 100906.

[13] G. Rosi, N. Auffray, Anisotropic and dispersive wave propagation within strain-gradient framework, Wave Motion 63 (2016) 120–134.

[14] G. Rosi, N. Auffray, Continuum modelling of frequency dependent acoustic beam focusing and steering in hexagonal lattices, European Journal of Mechanics – A/Solids 77 (2019) 103803.

[15] A. Lepidia, L. Bacigalupo, Multi-parametric sensitivity analysis of the band structure for tetrachiral acoustic metamaterials, International Journal of Solids and Structures 136–137 (2018) 186–202.

[16] A. Madeo, P. Neff, I. D. Ghiba, L. Placidi, G. Rosi, Wave propagation in relaxed micromorphic continua: modeling metamaterials with frequency band-gaps, Continuum Mechanics and Thermodynamics 27 (2015) 551–570.

[17] W. E. D. Nelissen, C. Ayas, C. Tekoğlu, 2D lattice material architectures for actuation, Journal of the Mechanics and Physics of Solids 124 (2019) 83–101.

[18] A. Vigliotti, V. S. Deshpande, D. Pasini, Non linear constitutive models for lattice materials, Journal of the Mechanics and Physics of Solids 64 (2014) 44–60.

[19] J. R. Greer, Materials by design: using architecture and nanomaterial size effects to attain unexplored properties, The Bridge 45 (2015) 37–44.

[20] L. R. Meza, A. J. Zelhofer, N. Clarke, A. J. Mateos, D. M. Kochmann, J. R. Greer, Resilient 3D hierarchical architected metamaterials, Proceedings of the National Academy of Sciences 112 (2015) 11502–11507.

[21] C. Bonatti, D. Mohr, Mechanical performance of additively-manufactured anisotropic and isotropic smooth shell-lattice materials: Simulations & experiments, Journal of the Mechanics and Physics of Solids 122 (2019) 1–26.

[22] A. Gross, P. Pantidis, K. Bertoldi, S. Gerasimidis, Correlation between topology and elastic properties of imperfect truss-lattice materials, Journal of the Mechanics and Physics of Solids 124 (2019) 577–598.

[23] M. R. O'Masta, L. Dong, L. St-Pierre, H. N. G. Wadley, V. S. Deshpande, The fracture toughness of octet-truss lattices, Journal of the Mechanics and Physics of Solids 98 (2017) 271–289.

[24] C. M. Portela, J. R. Greer, D. M. Kochmann, Impact of node geometry on the effective stiffness of non-slender three-dimensional truss lattice architectures, Extreme Mechanics Letters 22 (2018) 138–148.

[25] S. Khakalo, V. Balobanov, J. Niiranen, Modelling size-dependent bending, buckling and vibrations of 2D triangular lattices by strain gradient elasticity models: applications to sandwich beams and auxetics, International Journal of Engineering Science 127 (2018) 33–52.

[26] A. Desmoulins, D. M. Kochmann, Local and nonlocal continuum modeling of inelastic periodic networks applied to stretching-dominated trusses, Computer Methods in Applied Mechanics and Engineering 313 (2017) 85–105.

[27] E. Barchiesi, S. Khakalo, Variational asymptotic homogenization of beam-like square lattice structures, Mathematics and Mechanics of Solids, https://doi.org/10.1177/1081286519843155.

[28] M. G. Geers, V. V. Kouznetsova, W. A. Brekelmans, Multi-scale computational homogenization: Trends and challenges, Journal of Computational and Applied Mathematics 234 (2010) 2175–2182.

[29] S. Khakalo, J. Niiranen, Lattice structures as thermoelastic strain gradient metamaterials: Evidence from full-field simulations and applications to functionally step-wise-graded beams, Composites Part B: Engineering, https://doi.org/10.1016/j.compositesb.2019.107224.

[30] D. Shengyua, W. Weibin, F. Daining, A predictive micropolar continuum model for a novel three-dimensional chiral lattice with size effect and tension-twist coupling behavior, Journal of the Mechanics and Physics of Solids 121 (2018) 23–46.

[31] S. Khakalo, J. Niiranen, Form II of Mindlin's second strain gradient theory of elasticity with a simplification: For materials and structures from nano- to macro-scales, European Journal of Mechanics - A/Solids 71 (2018) 292–319.

[32] M. Poncelet, A. Somera, C. Morel, C. Jailin, N. Auffray, An experimental evidence of the failure of Cauchy elasticity for the overall modeling of a non-centro-symmetric lattice under static loading, International Journal of Solids and Structures 147 (2018) 223–237.

[33] A. Sridhar, V. G. Kouznetsova, M. G. D. Geers, Homogenization of locally resonant acoustic metamaterials towards an emergent enriched continuum, Computational Mechanics 57 (2016) 423–435.

[34] Y. Rahali, I. Giorgio, J. F. Ganghoffer, F. dell'Isola, Homogenization à la Piola produces second gradient continuum models for linear pantographic lattices, International Journal of Engineering Science 97 (2015) 148–172.

[35] F. dell'Isola, P. Seppecher, J. J. Alibert, T. Lekszycki, R. Grygoruk, M. Pawlikowski, D. Steigmann, I. Giorgio, U. Andreaus, E. Turco, M. Gołaszewski, N. Rizzi, C. Boutin, V. A. Eremeyev, A. Misra, L. Placidi, E. Barchiesi, L. Greco, M. Cuomo, A. Cazzani, A. D. Corte, A. Battista, D. Scerrato, I. Z. Eremeeva, Y. Rahali, J.-F. Ganghoffer, W. Müller, G. Ganzosch, M. Spagnuolo, A. Pfaff, K. Barcz, K. Hoschke, J. Neggers, F. Hild, Pantographic metamaterials: an example of mathematically driven design and of its technological challenges, Continuum Mechanics and Thermodynamics, https://doi.org/10.1007/s00161-018-0689-8.

[36] F. dell'Isola, P. Seppecher, M. Spagnuolo, E. Barchiesi, F. Hild, T. Lekszycki, I. Giorgio, L. Placidi, U. Andreaus, M. Cuomo, S. R. Eugster, A. Pfaff, K. Hoschke, R. Langkemper, E. Turco, R. Sarikaya, A. Misra, M. De Angelo, F. D'Annibale, A. Bouterf, X. Pinelli, A. Misra, B. Desmorat, M. Pawlikowski, C. Dupuy, D. Scerrato, P. Peyre, M. Laudato, L. Manzari, P. Göransson, C. Hesch, S. Hesch, P. Franciosi, J. Dirrenberger, F. Maurin, Z. Vangelatos, C. Grigoropoulos, V. Melissinaki, M. Farsari, W. Muller, B. E. Abali, C. Liebold, G. Ganzosch, P. Harrison, R. Drobnicki, L. Igumnov, F. Alzahrani, T. Hayat, Advances in pantographic structures: design, manufacturing, models, experiments and image analyses, Continuum Mechanics and Thermodynamics, https://doi.org/10.1007/s00161-019-00806-x.

[37] R. D. Mindlin, Micro-structure in linear elasticity, Archive for Rational Mechanics and Analysis 16 (1964) 51–78.

[38] H. Tang, Y. Dong, T. Wang, Y. Dong, Simulation of strain localization with discrete element-Cosserat continuum finite element two scale method for granular materials, Journal of the Mechanics and Physics of Solids 122 (2019) 450–471.

[39] P. Poorsolhjouy, A. Misra, Granular micromechanics based continuum model for grain rotations and grain rotation waves, Journal of the Mechanics and Physics of Solids 129 (2019) 244–260.

[40] S. Forest, Homogenization methods and mechanics of generalized continua - part 2, Theoretical and Applied Mechanics 28–29 (2002) 113–144.

[41] D. K. Trinh, R. Janicke, N. Auffray, S. Diebels, S. Forest, Evaluation of generalized continuum substitution models for heterogeneous materials, International Journal for Multiscale Computational Engineering 10 (6) (2012) 527–549.

[42] R. Jänicke, H. Steeb, Minimal loading conditions for higher-order numerical homogenisation schemes, Archive of Applied Mechanics 123 (2012) 1075–1088.

[43] D. Bigoni, W. J. Drugan, Analytical derivation of Cosserat moduli via homogenization of heterogeneous elastic materials, Journal of Applied Mechanics 74 (2006) 741–753.

[44] J. Altenbach, H. Altenbach, V. A. Eremeyev, On generalized Cosserat-type theories of plates and shells: a short review and bibliography, Archive of Applied Mechanics 80 (2010) 73–92.

[45] A. Misra, P. Poorsolhjouy, Identification of higher-order elastic constants for grain assemblies based upon granular micromechanics, Mathematics and Mechanics of Complex Systems 3 (2015) 285–308.

[46] R. Biswas, L. H. Poh, A micromorphic computational homogenization framework for heterogeneous materials, Journal of the Mechanics and Physics of Solids 102 (2017) 187–208.

[47] G. Hütter, Homogenization of a cauchy continuum towards a micromorphic continuum, Journal of the Mechanics and Physics of Solids 99 (2017) 394–408.

[48] O. Rokoš, M. M. Ameen, R. H. J. Peerlings, M. G. D. Geers, Micromorphic computational homogenization for mechanical metamaterials with patterning fluctuation fields, Journal of the Mechanics and Physics of Solids 123 (2019) 119–137.

[49] L. Placidi, U. Andreaus, A. D. Corte, T. Lekszycki, Gedanken experiments for the determination of two-dimensional linear second gradient elasticity coefficients, Zeitschrift für angewandte Mathematik und Physik 66 (2015) 3699–3725.

[50] H. Nassar, Q.-C. He, N. Auffray, On asymptotic elastodynamic homogenization approaches for periodic media, Journal of the Mechanics and Physics of Solids 88 (2016) 274–290.

[51] L. Placidi, U. Andreaus, I. Giorgio, Identification of two-dimensional pantographic structure via a linear D4 orthotropic second gradient elastic model, Journal of Engineering Mathematics 103 (1) (2017) 1–21.

[52] A. T. Karttunen, J. Reddy, J. Romanoff, Two-scale constitutive modeling of a lattice core sandwich beam, Composites Part B: Engineering 160 (2019) 66–75.

[53] A. T. Karttunen, J. Reddy, J. Romanoff, Two-scale micropolar plate model for web-core sandwich panels, International Journal of Solids and Structures 170 (2019) 82–94.

[54] V. A. Eremeyev, H. Altenbach, On the Direct Approach in the Theory of Second Gradient Plates, Vol. 45, Springer, 2015, pp. 147–154.

[55] H. Altenbach, V. Eremeyev, Shell-like Structures: Advanced Theories and Applications, CISM International Centre for Mechanical Sciences, Springer, 2016. doi:10.1007/978-3-319-42277-0.

[56] H.-T. Thai, T. P. Vo, T.-K. Nguyen, S.-E. Kim, A review of continuum mechanics models for size-dependent analysis of beams and plates, Composite Structures 177 (2017) 196–219.

[57] J. Niiranen, A. H. Niemi, Variational formulation and general boundary conditions for sixth-order boundary value problems of gradient-elastic Kirchhoff plates, European Journal of Mechanics - A/Solids 61 (2017) 164–179.

[58] J. Niiranen, J. Kiendl, A. H. Niemi, A. Reali, Isogeometric analysis for sixth-order boundary value problems of gradient-elastic Kirchhoff plates, Computer Methods in Applied Mechanics and Engineering 316 (2017) 328–348.

[59] J. Niiranen, V. Balobanov, J. Kiendl, S. Hosseini, Variational formulations, model comparisons and isogeometric analysis for Euler-Bernoulli micro- and nano-beam models of strain gradient elasticity, Mathematics and Mechanics of Solids 24 (2019) 312–335.

[60] V. Balobanov, J. Niiranen, Locking-free variational formulations and isogeometric analysis for the Timoshenko beam models of strain gradient and classical elasticity, Computer Methods in Applied Mechanics and Engineering 339 (2018) 137–159.

[61] S. T. Yaghoubi, V. Balobanov, S. M. Mousavi, J. Niiranen, Variational formulations and isogeometric analysis for the dynamics of anisotropic gradient-elastic Euler–Bernoulli and shear-deformable beams, European Journal of Mechanics - A/Solids 69 (2018) 113–123.

[62] V. Balobanov, J. Kiendl, S. Khakalo, J. Niiranen, Kirchhoff–Love shells within strain gradient elasticity: weak and strong formulations and an H^3-conforming isogeometric implementation, Computer Methods in Applied Mechanics and Engineering 344 (2019) 837–857.

[63] J. Niiranen, S. Khakalo, V. Balobanov, A. H. Niemi, Variational formulation and isogeometric analysis for fourth-order boundary value problems of gradient-elastic bar and plane strain/stress problems, Computer Methods in Applied Mechanics and Engineering 308 (2016) 182–211.

[64] S. Khakalo, J. Niiranen, Isogeometric analysis of higher-order gradient elasticity by user elements of a commercial finite element software, Computer-Aided Design 82 (2017) 154–169.

[65] S. Khakalo, J. Niiranen, Gradient-elastic stress analysis near cylindrical holes in a plane under bi-axial tension fields, International Journal of Solids and Structures 110–111 (2017) 351–366.

[66] J. Niiranen, S. Khakalo, V. Balobanov, Isogeometric finite element analysis of mode I cracks within strain gradient elasticity, Journal of Structural Mechanics 50 (2017) 337–340.

[67] J. Réthoré, C. Kaltenbrunner, T. B. T. Dang, P. Chaudet, M. Kuhn, Gradient-elasticity for honeycomb materials: Validation and identification from full-field measurements, International Journal of Solids and Structures 72 (2015) 108–117.

[68] G. Barbagallo, D. Tallarico, M. V. D'Agostino, A. Aivaliotis, P. Neff, A. Madeo, Relaxed micromorphic model of transient wave propagation in anisotropic band-gap metastructures, International Journal of Solids and Structures 162 (2019) 148–163.

[69] M. Lazar, G. Po, The non-singular Green tensor of Mindlin's anisotropic gradient elasticity with separable weak non-locality, Physics Letters A 379 (24-25) (2015) 1538–1543.

[70] S. M. Mousavi, J. N. Reddy, J. Romanoff, Analysis of anisotropic gradient elastic shear deformable plates, Acta Mechanica 227 (2016) 3639–3656.

[71] C. Polizzotto, Anisotropy in strain gradient elasticity: Simplified models with different forms of internal length and moduli tensors, European Journal of Mechanics - A/Solids 71 (2018) 51–63.

[72] E. C. Aifantis, On the role of gradients in the localization of deformation and fracture, International Journal of Engineering Science 30 (1992) 1279–1299.

[73] C. Q. Ru, E. C. Aifantis, A simple approach to solve boundary-value problems in gradient elasticity, Acta Mechanica 101 (1993) 59–68.

[74] B. S. Altan, E. C. Aifantis, On some aspects in the special theory of gradient elasticity, Journal of the Mechanical Behavior of Materials 8 (1997) 231–282.

[75] A. I. Borovkov, Effective physical and mechanical properties of fiber composites (in Russian), M.: Изд-во ВИНИТИ, 1985.

[76] N. Auffray, Q. C. He, H. L. Quang, Complete symmetry classification and compact matrix representations for 3D strain gradient elasticity, International Journal of Solids and Structures 159 (2019) 197–210.

[77] N. Auffray, H. L. Quang, Q. He, Matrix representations for 3D strain-gradient elasticity, Journal of the Mechanics and Physics of Solids 61 (2013) 1202–1223.

[78] T. J. R. Hughes, J. A. Cottrell, Y. Bazilevs, Isogeometric analysis: Cad, finite elements, nurbs, exact geometry and mesh refinement, Computer Methods in Applied Mechanics and Engineering 194 (2005) 4135–4195.

[79] L. Beirão da Veiga, T. Hughes, J. Kiendl, C. Lovadina, J. Niiranen, A. Reali, H. Speleers, A locking-free model for Reissner–Mindlin plates: Analysis and isogeometric implementation via NURBS and triangular NURPS, Math. Meth. Apll. Sci. 25 (2015) 1519–1551.

[80] A. Iltchev, V. Marcadon, S. Kruch, S. Forest, Computational homogenisation of periodic cellular materials: Application to structural modelling, International Journal of Mechanical Sciences 93 (2015) 240–255.

[81] Z.-P. Wang, L. H. Poh, J. Dirrenberger, Y. Zhu, S. Forest, Isogeometric shape optimization of smoothed petal auxetic structures via computational periodic homogenization, Computer Methods in Applied Mechanics and Engineering 323 (2017) 250–271.

[82] J. N. Reddy, Mechanics of Laminated Composite Plates and Shells. Theory and Analysis, CRC Press, 2004.

[83] J.-M. Cardona, S. Forest, R. Sievert, Towards a theory of second grade thermoelasticity, Extracta Mathematicae 14 (1999) 127–140.

[84] A. Javili, F. dell'Isola, P. Steinmann, Geometrically nonlinear higher-gradient elasticity with energetic boundaries, Journal of the Mechanics and Physics of Solids 61 (2013) 2381–2401.

[85] L. Placidi, E. Barchiesi, Energy approach to brittle fracture in strain-gradient modelling, Proceedings of the Royal Society A: Mathematical, Physical and Engineering Sciences 474 (2018) 20170878.

[86] R. G. Cowper, The shear coefficient in Timoshenko's beam theory, Journal of Applied Mechanics 33 (1966) 335–340.